8-1-2012

Design and analysis of a UHF transmission line coupler for telemetry and power harvesting in a passive sensor system

Jean-Jacques DeLisle

Design and Analysis of a UHF Transmission Line Coupler for Telemetry and Power Harvesting in a Passive Sensor System

by

Jean-Jacques DeLisle

A Thesis Submitted

in

Partial Fulfillment

of the

Requirements for the Degree of

MASTER OF SCIENCE

in

Electrical Engineering

Approved by:

PROF._____

(Dr. Robert Bowman, Advisor)

PROF._____

(Dr. Borkholder, Committee Member)

PROF._____

(Dr. Tsouri, Committee Member)

PROF._____

(Dr. Sohail A. Dianat, Department Head)

DEPARTMENT OF ELECTRICAL AND MICROELECTRONIC ENGINEERING

KATE GLEASON COLLEGE OF ENGINEERING

ROCHESTER INSTITUTE OF TECHNOLOGY

ROCHESTER, NEW YORK

August, 2012

Acknowledgements

Abstract

The intra-coaxial transmission line coupler TXC is a four port device designed to harvest power from a host coaxial transmission line and to provide telemetry for remote sensing applications via the same host transmission line. Seven different TXC structures were designed and fabricated to study the effects of varying specific geometric features on the electrical characteristics of the TXC. Each TXC structure was tested using a RF vector network analyzer and analyzed using a commercially available finite-element numerical simulator. Two main observations resulted from the study: 1) the resonant frequency depends mainly on the value of the tuning capacitor and the loop inductance of the TXC, and 2) the electrical characteristics are relatively insensitive to variations in all geometric features except the TXC loop surface area and, to a lesser extent, the separation distance between the coax center conductor and the TXC loop. It was found that the output impedance, Q-factor, voltage transfer characteristic, and power transfer characteristic computed from simulations were systematically greater than those computed from experiment. It was shown that by using experimental results to "fit" the simulations, a much better agreement could be obtained between experimental and simulation results.

Table of Contents

List of Abbreviations

PSN	Passive Sensor Node
TXC	Transmission Line Coupler
RF	Radio Frequency
TEM	Transverse Electromagnetic
NF	Near Field
DC	Directional Coupler
RFID	Radio Frequency Identification
I-C	Intra-coaxial
TX	Transmission
S Parameter	Scattering Parameter
Z Parameter	Impedance Parameter
Z_O	Characteristic Impedance
IC	Integrated Circuit
VTC	Voltage Transfer Characteristic
IMN	Impedance Matching Network
Z_{34_IN}	The differential input impedance between Port 3 & Port 4 of the TXC
P_{TC}	Power Transfer Characteristic
V_{TC}	Voltage Transfer Characteristic
f_r	Resonant Frequency
Q Factor	Quality Factor
HZ	Hertz
BW	Bandwidth
RLC	Resistance Inductance Capacitance
R	Resistance
L	Inductance
C	Capacitance
Y	Skin Effect Modulus
LDS	Laser Defined Structuring
LCP	Liquid Crystal Polymer
VNA	Vector Network Analyzer
3D	Three Dimensional
PCB	Printed Circuit Board
DIN	Deutsches Institut für Normung (German Institute of Standards)
N (type)	Niell (named after Paul Niell)
SMB	Sub miniature B
3mm	Three millimeter (RF standard cable size)
pF	Pico-Farads
CF	Coupling Factor
HFSS	High frequency structural simulator
CAD	Computer Aided Design

Chapter 1 Introduction

The RF (radio frequency) coaxial cable is a specialized controlled impedance medium used to transmit RF, video, high speed data, or precision measurement signals. The coaxial cable is configured with an insulated center conductor separated from a concentric shield providing an isolated and stable transmission medium. Sections of coaxial cable are connected together using RF connectors. RF connectors are designed to maintain the electrical shielding and characteristic impedance of the coaxial cable system. The telecommunications industry uses millions of RF connectors every year to interconnect sections of coaxial cables. The two primary failure modes in cellular tower RF connectors are connectors becoming loose and connector moisture ingress. Either condition can significantly alter the characteristic impedance of the RF transmission line and cause system degradation or catastrophic failure. In spite of considerable improvements in connector design, RF connector failures continue to plague the telecommunications industry.

An intra-coaxial passive sensing node (PSN) has been developed to detect the dominant failure mechanisms in RF coaxial connectors. In addition, the PSN monitors the quality of propagating RF signals in the coaxial cable, harvests RF energy from the coaxial cable, and provides a telemetry technology to report both the system status and unique identification of each connector PSN. Degrading quality in an RF connector can be detected and corrected before catastrophic system failure occurs.

An essential feature of the PSN is the transmission line coupler structure (TXC). The TXC is a metallic loop structure that couples electromagnetically with the RF fields inside the coaxial cable. Energy harvesting, signal integrity monitoring, and telemetry all depend on this coupling structure. RFID is well-known in the literature [1]-[7] as a means of RF communication with small antennas in the far-field or near-field of a remote transmitter. However, it does not describe the energy coupling of the intra-

coaxial TXC.   The RF energy present in a coaxial transmission line propagates as a TEM waveguide mode and not as free radiation as in an RFID transmitter.

The TXC resembles the port structure and shares some of the performance characteristics of a classic four-port directional coupler (DC) [8]-[9] with ports 1 and 2 connecting the main line and ports 3 and 4 the coupled line. Like a DC that uses a small coupling factor of 30 dB, the TXC achieves low main line insertion loss and return loss. However, the TXC does not attempt to match the coupled port (ports 3 and 4) impedances with the main line port (ports 1 and 2) impedances like a DC. A resonant impedance is formed between the coupled ports on the TXC. This approach compromises coupler directivity and coupling flatness in frequency response when compared to a DC but achieves the desired level of power harvesting at a specified resonant frequency.

The goal of this thesis is to understand the operating characteristics of the TXC related to its geometric form and provide some simple guidelines for designing an intra-coaxial TXC.   This work will include designing, fabricating, and measuring experimentally the electrical characteristics of several different TXC devices. The shapes of the devices are varied in order to examine the influence of geometry on the electrical behavior. A finite-element numerical simulator, Ansys Corporation's High Frequency Structural Simulator (HFSS™), is also used to explore the relationship between geometry and electrical behavior.   Parameters extracted from the experimental measurements are used to fit the numerical simulation.

This thesis provides insights that will enable the development of a compact engineering model for the TXC.   Such a model would be useful in simulating the performance of a PSN-based telecommunications system. As a first step, a compact mathematical model for the TXC has been developed [11]. This model requires several parameters that must be provided either from experimental results or from numerical simulation. This thesis represents an initial attempt to establish the relationship between geometry and the value of parameters for the mathematical model.

The contributions of this thesis are: preliminary simulations on TXC structures to verify system performance requirements, designed TXC test structures to verify preliminary simulations and to explain new areas of resonant frequency power harvesting and telemetry, developed a test protocol and test system to conduct laboratory and simulation testing, analyzed measurements results and compared them to system requirements.

This thesis is organized as follows:

Chapter 2 contains a detailed physical description of the PSN system and discusses the desired behavior of the TXC.

The analysis approach for the TXC is outlined in Chapter 3 and describes the requirements for optimizing power transfer in the system, and details the figures of merit critical to operation of TXC.

The physical constraints imposed by the PSN system are described in Chapter 4. This section details how the constraints influence the geometry of the TXC, and how this study can be used to provide an understanding of the mathematical model parameters of the TXC.

Chapter 5 contains a detailed description of the test fixture, the Vector Network Analyzer (VNA) instrument used to measure the electrical characteristics, the experimental procedure used to perform the geometric study, and details associated with the HFSS simulations. The contribution of a customized test protocol, fixtures, and structures is described here.

The results of the experiment and HFSS simulations are described in Chapter 6. The contribution of measurement results is described here.

Chapter 7 includes a discussion of the experimental and HFSS results along with a discussion of a means of calibrating the HFSS results using the experimental data. The analysis contribution of the geometric study is provided here.

Concluding remarks appear in Chapter 8. This chapter also presents an outline for future work based upon the findings of this thesis, including how foundational knowledge of the TXC can be used to enable parameter extraction for the engineering model.

Chapter 2: System Description

The PSN, outlined in Chapter 1, utilizes the coaxial transmission line as a source of RF energy as well as a communications path for sensor data it acquires at the node (i.e., the coaxial connector). The PSN system is designed to sense temperature, coaxial connector tightness, signal integrity, and relative humidity within the coaxial connector. This information is critical in failure mode detection, prediction, and transmission line repair.

A top level diagram of the PSN system incorporated into a industrial telecommunications system is provided in Fig. 2-1. The PSN TX (Transceiver) is connected to the telecom. system by a directional coupler so that is can send the PSN power tone, a power and communications carrier tone, through the coaxial line to the remote PSN systems through port 1 to port 2. This power tone provides energy for the PSN system at an exact telecom. test frequency in short bursts to power and communicate with the PSN system. The power tone is then modulated by the PSN, and the modulated reflections of the power tone are received by the PSN TX, through port 3, and converted into data readings of the sensors from the PSN system. Port 4 couples the outgoing TX from the PSN TX and can be used to isolate the modulated signal reflected by the PSN.
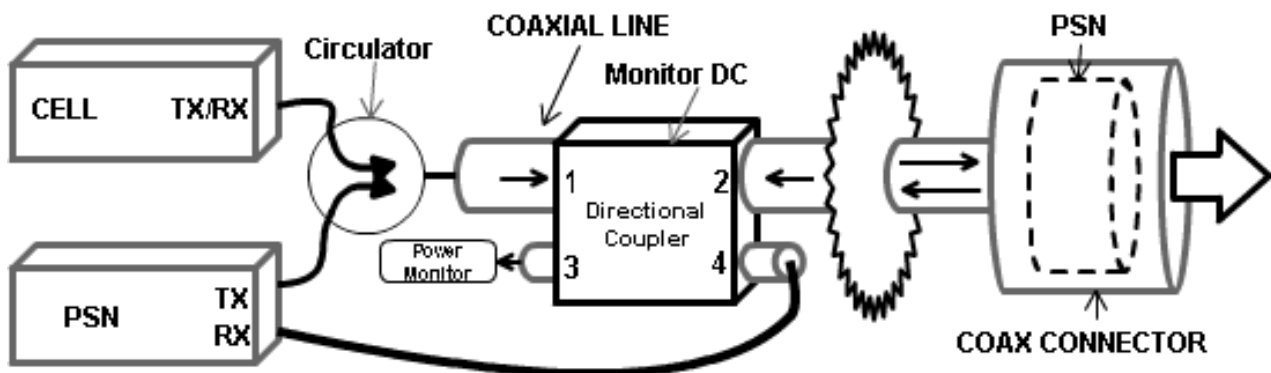

Fig. 2-1: A top level diagram of the PSN system incorporated into a pre-existing telecommunications system.

The coaxial cables are controlled impedance transmission lines used in industrial telecommunication systems usually consisting of inner and outer conductors constructed of a highly conductive metal, such as copper and dielectric spacers. Connectors consisting of dielectric filler and brass conductors are attached to the coaxial cables using specially designed press fit metal parts. The PSN system is designed to be compatible with these types of connectors to avoid any corruption of the telecommunications operations of the coaxial transmission line. This requires that the PSN be completely contained within the connector housing and be loosely coupled to the transmission line so that no significant change is induced in the RF operation. Fig. 2-2 shows an example diagram of the TXC system including the connection to the integrated circuit (IC) which provides the electronic signal processing.
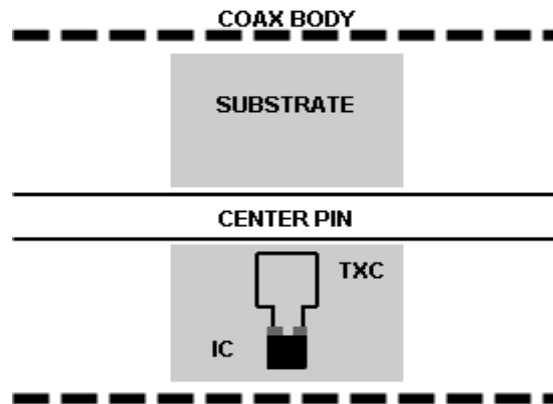
Fig. 2-2: A TXC loop structure with integrated circuit (IC) is shown in a coaxial cross section with a substrate internal to the coaxial system.

Components of the PSN are physically supported by a platform which must have the ability to be manufactured with very accurate metal traces for electric circuitry. The requirements of coaxial transmission line operation place additional constraints on dielectric properties of the platform. A type of plastic that can be metallized, has the correct dielectric properties, and can be consistently and accurately molded to a required shape to support all of the PSN functions is a liquid crystal polymer (LCP) plastic. Fine line metallurgy is patterned on the surface with a laser defined structuring (LDS) process. More details of this material and the manufacturing process are given in Chapter 4. Fig. 2-3 and Fig. 2-4 show 3D CAD models of a PSN molded interconnect device (MID) substrate with a complex metallized TXC

structure and an IC landing zone, respectively. Fig. 2-5 shows a picture of a real TXC structure and substrate.

Fig. 2-3: A 3D CAD model of a MID with complex TXC loop structure. The scale is in millimeters.
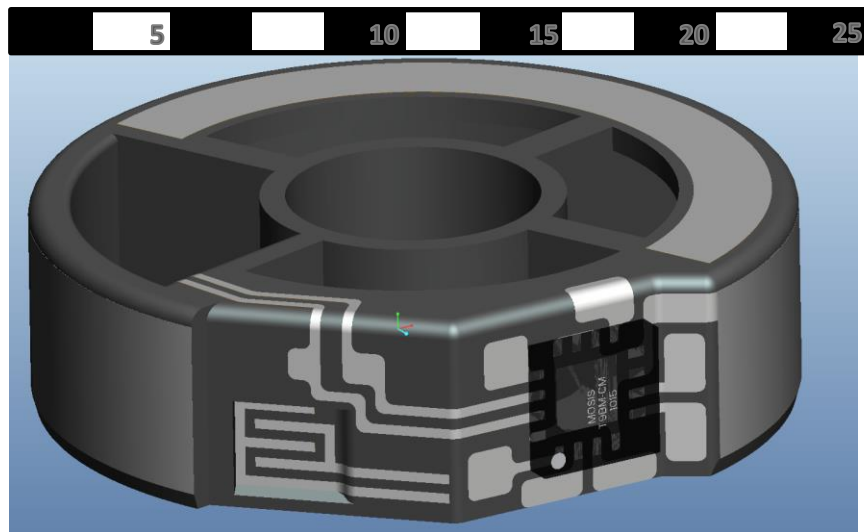
Fig. 2-4: A 3D CAD model of the MID showing the IC landing zone with IC package and patterned metallization for sensor applications. The scale is in millimeters.
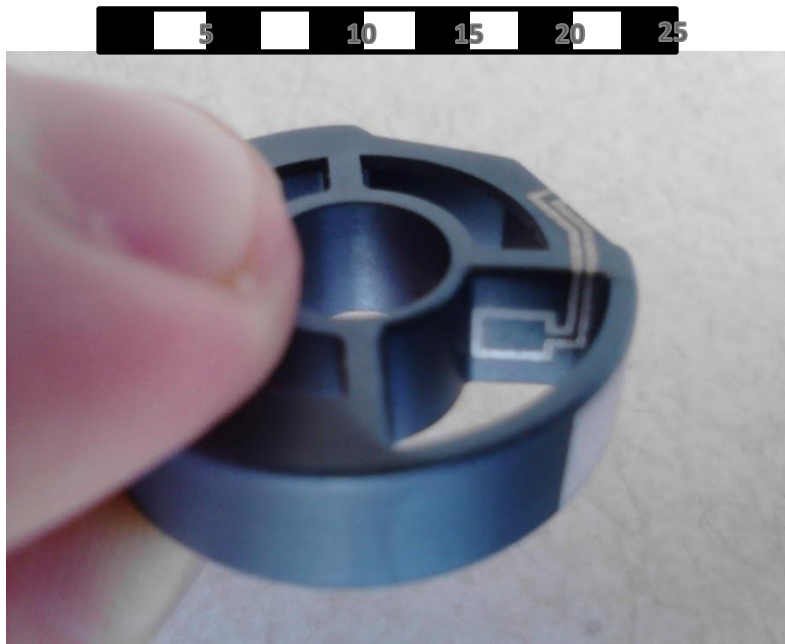
Fig. 2-5: A picture of a TXC loop structure and substrate. The scale is in millimeters.

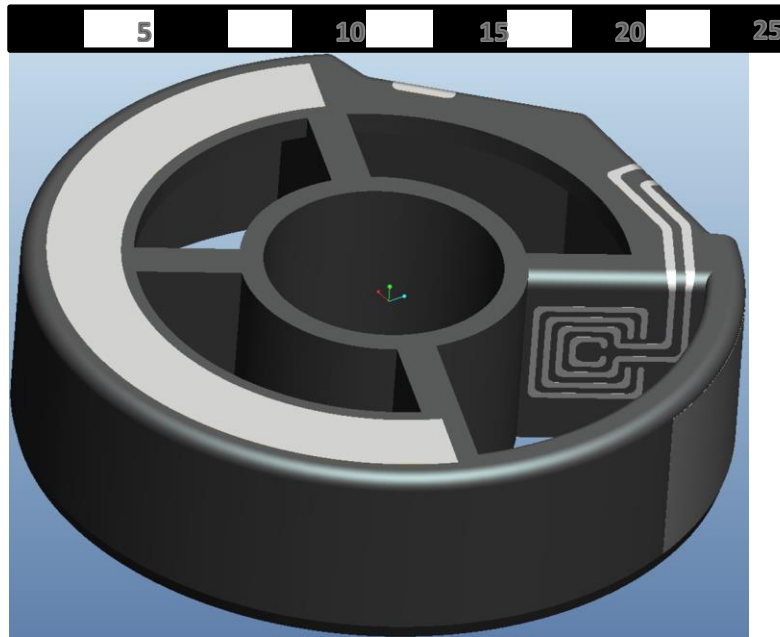The final molded interconnect device (MID) platform includes an integrated circuit (IC) that is the brains of the PSN system, and a transmission line coupler (TXC). The desired behavior of the TXC is to exhibit weak coupling with the host transmission line at all frequencies except for those frequencies near a predefined resonance. This resonant frequency is the power tone frequency and is determined primarily by the tuning capacitor of the TXC. It is the frequency at which the PSN harvests power from the host transmission line and communicates sensor information to the base station.

The PSN IC places a number of requirements on the coupling characteristics of the TXC. The TXC must exhibit adequate resonant voltage and impedance at its terminals. It must provide adequate power for the IC and must be precisely tunable to the power tone resonant frequency with limited power from the PSN network transmitter (~3 W). Finally, the TXC must fit in the limited form factor available in the host coaxial connector. To be precise the power tone frequency is 846.5 MHZ a frequency designated by the carriers for testing, the power requirement to the PSN IC is 300 uW, the voltage requirement is a minimum of 1.5 V, and the resonant output impedance requirement of the TXC is approximately 1 kΩ. Details about how this is accomplished are covered in Chapters 3, 4, and 5.

Chapter 3 Electrical Characteristics of the TXC

The TXC is treated as part of a RF four port network. This network can be modeled as two coupled transmission lines: one being a segment of the host coaxial transmission line and the other being a segment of transmission line which is part of the TXC. A diagram representing coupled transmission lines is provided in Fig. 3-1 with indicators for the incident power (a subscripts) and reflected power (b subscripts) in the four port network. It can be observed that the four port network has a common ground return path for both the TXC and the coaxial line.
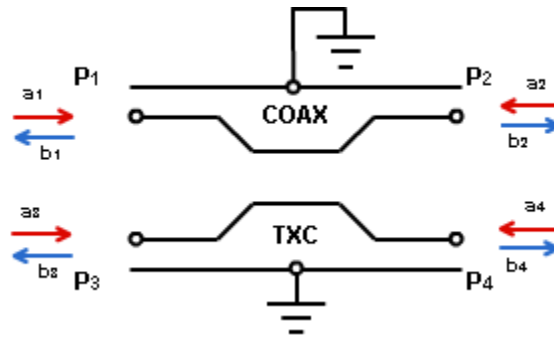
Fig. 3-1: A coupled transmission line model of the host transmission line and TXC

The S-matrix relates the incident and reflected power at all terminals as shown in Eq. (3-1).

$$\begin{bmatrix} b_1 \\ b_2 \\ b_3 \\ b_4 \end{bmatrix} = \begin{bmatrix} S_{11} & S_{12} & S_{13} & S_{14} \\ S_{21} & S_{22} & S_{23} & S_{24} \\ S_{31} & S_{32} & S_{33} & S_{34} \\ S_{41} & S_{42} & S_{43} & S_{44} \end{bmatrix} \begin{bmatrix} a_1 \\ a_2 \\ a_3 \\ a_4 \end{bmatrix}$$

(3-1)

It is assumed in this thesis that the TXC network is symmetric about a plane that is perpendicular to the direction of propagation and passes through the center of the coupled transmission lines. This assumption allows for a reduction in the number of independent matrix elements of the S-matrix terms [11]. The six

independent S-parameters (Scattering parameters) are taken to be S_{11}, S_{12}, S_{13}, S_{14}, S_{33}, and S_{34} as shown in Eq. (3-2)

$$\begin{bmatrix} S_{11} & S_{12} & S_{13} & S_{14} \\ S_{21} & S_{22} & S_{23} & S_{24} \\ S_{31} & S_{32} & S_{33} & S_{34} \\ S_{41} & S_{42} & S_{43} & S_{44} \end{bmatrix} \xRightarrow{symmetrical} \begin{bmatrix} S_{11} & S_{12} & S_{13} & S_{14} \\ S_{12} & S_{11} & S_{14} & S_{13} \\ S_{13} & S_{14} & S_{33} & S_{34} \\ S_{14} & S_{13} & S_{34} & S_{33} \end{bmatrix}$$

(3-2)

Fig. #3-2 shows spectral plots of the six independent S-parameters for a typical TXC. **S_{11}** typically averages around -30dB and is a measure of the reflected energy at Port 1 due to incident energy at Port 1. **S_{12}** is near 0 dB across the frequency spectrum and measures energy exiting Port 1 due to incident energy on Port 2. **S_{13}** measures the energy exiting Port 1 due to the incident energy on Port 3. **S_{14}** measures energy exiting Port 1 due to the incident energy on Port 4. **S_{13}** and **S_{14}** show the resonant behavior of the TXC structure with a significant increase in energy coupling around the resonant point. **S_{33}** is the reflected energy measured at Port 3 due to incident energy on Port 3. **S_{34}** is energy exiting Port 3 due to incident energy at Port 4.
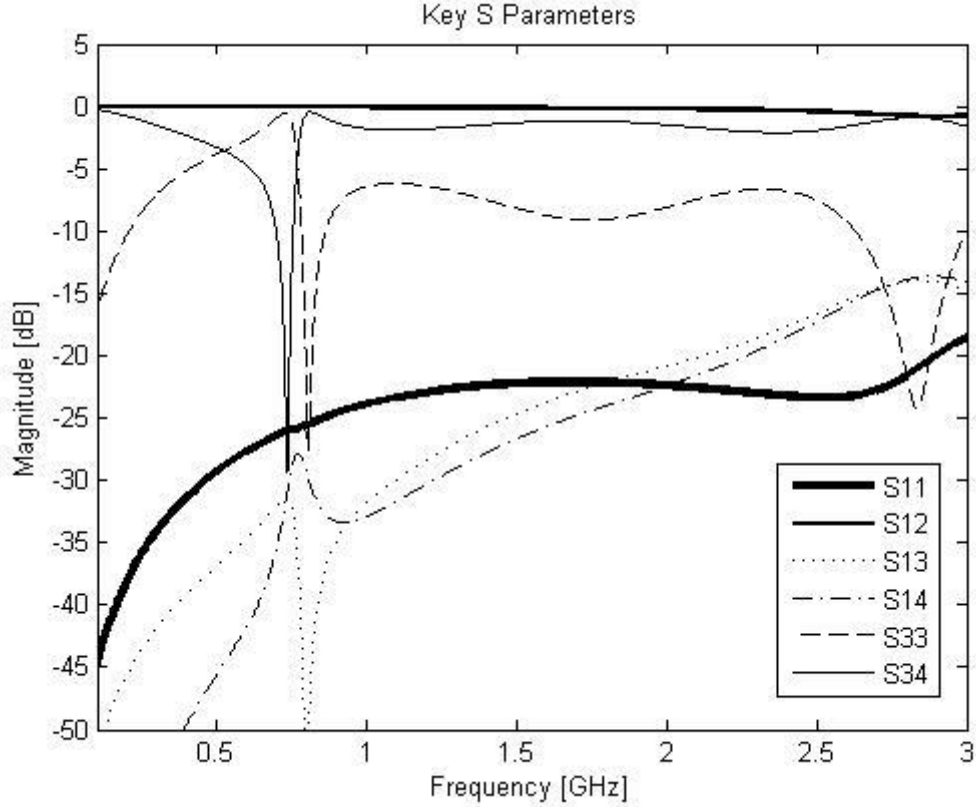
Fig. 3-2: Spectral behavior of the six key S parameters for a typical symmetrical four port TXC.

Several useful electrical terminal characteristics of the TXC such as voltages, currents, and impedances can be expressed more easily in terms of Z-parameters. In order to compute these quantities the S-matrix must first be converted into Z-matrix (impedance matrix). Z-parameters can be derived from the *S*-parameters described in Eq. (3-1) using Eq. (3-3).

$$\mathbf{Z} = \sqrt{\mathbf{Z}_O}\ (\mathbf{I}-\mathbf{S})^{-1}(\mathbf{I}+\mathbf{S})\ \sqrt{\mathbf{Z}_O}$$

(3-3)

where

$$\mathbf{Z}_O = \begin{bmatrix} Z_{01} & 0 & 0 & 0 \\ 0 & Z_{02} & 0 & 0 \\ 0 & 0 & Z_{03} & 0 \\ 0 & 0 & 0 & Z_{04} \end{bmatrix}.$$

(3-4)

11

In Eq. (3-4) Z_{01}, Z_{02}, Z_{03}, and Z_{04} are the port impedances. A simplification can be made with this equation assuming all ports have the same characteristic impedance, Z_0, at the port terminals:

$$Z = Z_O(I-S)^{-1}(I+S)$$

(3-5)

Fig. 3-3 shows a spectral plot of the Z-parameters derived from the S-parameters shown in Fig. 3-2 using Eq. (3-5).
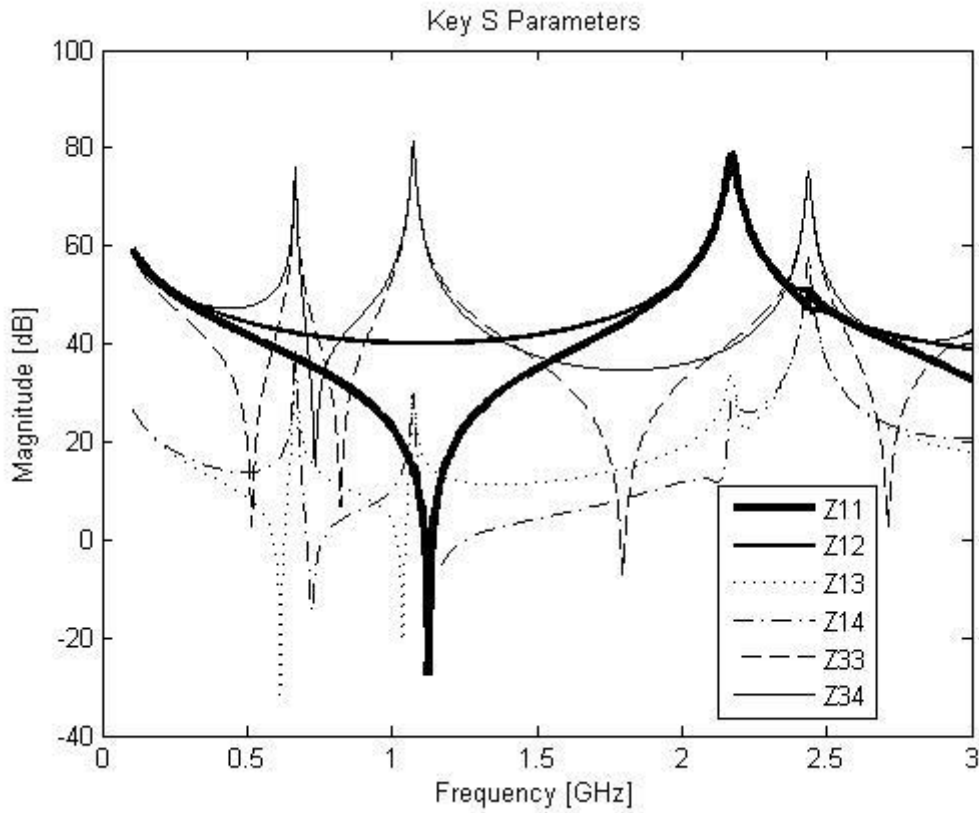
Fig. 3-3: Spectral behavior of the six key Z parameters for a typical symmetrical four port TXC.

Fig. *3-4* shows the TXC incorporated in a network. An RF input voltage with a matched generator impedance, $Z_G = Z_O$ is used to stimulate Port 1. Port 2 is terminated with an impedance Z_O. The generator impedance and termination impedance for Ports 1 and 2 are made equal to Z_O to allow for maximum power transfer and to minimize reflections. Ports 3 and 4 are connected through a load impedance Z_L that replaces the IC interface in the network. Equations can be derived in terms of the TXC Z-parameters that describe terminal impedance, power transfer, and voltage characteristics for this

12

network. These characteristics are useful in the analysis of the TXC since they demonstrate the key characteristics considered when designing an IC that provides the functionality of the PSN system.
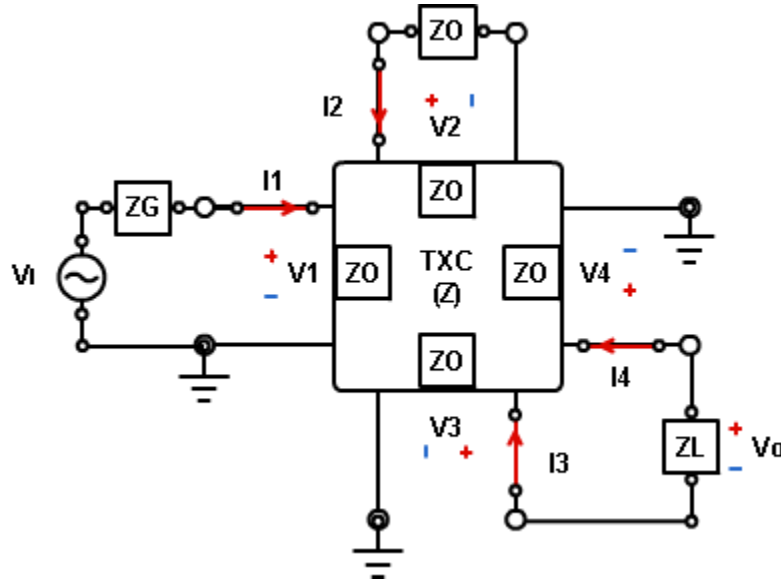
Fig. 3-4: A four port Z parameter network is shown representing the TXC system.

The differential terminal input impedance Z_{34IN} is useful in understanding the electrical behavior of the TXC in that it incorporates the characteristics of all six independent S-parameters. It is critical in designing PSN circuits since the functions of power harvesting and telecommunications depend on impedance-matching Z_{34IN} to the IC in order to achieve effective power transfer at resonance. An impedance matching network (IMN) must be used for maximum power transfer and to minimize the RF "presence" of the IC-TXC system due to reflections. In order to design an optimized IMN, Z_{34IN} must be accurately modeled. As shown in [11], Z_{34IN} for a symmetric TXC can be expressed in terms of Z-parameters according to the following equation.

$$Z_{34IN} = \frac{1}{2}\left(Z_{33} - Z_{34} - \frac{(Z_{13} - Z_{14})^2}{Z_O + Z_{11} - Z_{12}}\right)$$

(3-6)

The voltage transfer characteristic, V_{TC}, is a measure of the output voltage at Ports 3 and 4 when a voltage is supplied with a generator at Port 1. The resonant V_{TC} is used to gauge the ability of a TXC structure to supply voltage to power the IC of the PSN. If the voltage supplied to the IC is too low, it will

13

not be able to operate. On the other hand, a high output voltage means that less circuitry is needed (such as a voltage doubler) in the IC to condition the input power, which results in a more efficient, robust, and inexpensive IC.

The voltage transfer characteristic and power transfer characteristic (P_{TC}) can also be expressed in terms of TXC Z-parameters. The derivation for V_{TC} and P_{TC} begins with the definition of the **Z**-matrix:

$$\begin{bmatrix} V_1 \\ V_2 \\ V_3 \\ V_4 \end{bmatrix} = \begin{bmatrix} Z_{11} & Z_{12} & Z_{13} & Z_{14} \\ Z_{21} & Z_{22} & Z_{23} & Z_{24} \\ Z_{31} & Z_{32} & Z_{33} & Z_{34} \\ Z_{41} & Z_{42} & Z_{43} & Z_{44} \end{bmatrix} \begin{bmatrix} I_1 \\ I_2 \\ I_3 \\ I_4 \end{bmatrix} \Rightarrow \mathbf{V} = \mathbf{ZI}$$

(3-6)

V_{TC} and P_{TC}, are found by applying basic electrical analysis techniques to the system of equations shown in Eq. (3-6). Eq. (3-7) are obtained from Eq. (3-6) by substituting $I_4 = -I_3$ (see Fig. *3-4*):

$$V_1 = Z_{11}I_1 + Z_{12}I_2 + Z_{13}I_3 - Z_{14}I_3$$
$$V_2 = Z_{21}I_1 + Z_{22}I_2 + Z_{23}I_3 - Z_{24}I_3$$
$$V_3 = Z_{11}I_1 + Z_{32}I_2 + Z_{33}I_3 - Z_{34}I_3$$
$$V_4 = Z_{11}I_{11} + Z_{42}I_2 + Z_{43}I_3 - Z_{44}I_1$$

(3-7)

The following relations result from circuit analysis of the network shown in Fig. *3-4*: $\mathbf{V_1} = \mathbf{V_I} - \mathbf{Z_O}/\mathbf{I_1}$ and $\mathbf{I_3} = -\mathbf{V_O}/\mathbf{Z_L}$. After substitution of these relations, the system of equations, Eq. (3-7) can be easily solved with a symbolic manipulator such as MATLAB Symbolic Toolbox. The result is V_{TC}, which has been simplified by taking advantage of the assumed symmetry of the TXC network (see Eq. (3-2)):

$$\frac{V_O}{V_I} = \frac{N}{D_1 - D_2}$$

$$N = Z_L(Z_{13} - Z_{14})$$

$$D_1 = 4Z_{13}Z_{14} + 2Z_OZ_{33} + 2Z_{11}Z_{33} + 2Z_{12}Z_{34} + Z_OZ_L + Z_{11}Z_L$$

$$D_2 = 2Z_{13}^2 + 2Z_{14}^2 + 2Z_OZ_{34} + 2Z_{11}Z_{34} + 2Z_{12}Z_{33} + Z_{12}Z_L \tag{3-8}$$

Using Eq. (3-8) an exact value for $\mathbf{V_{TC}} = \mathbf{V_O}/\mathbf{V_I}$ can be calculated as a function of TXC Z- parameters.

The power transfer characteristic, P_{TC}, is a measure of the output power between Ports 3 and 4 when a generator supplies power at Port 1. The availability of power at the outputs of the TXC structure is required for the operation of the IC in the PSN system. P_{TC} can be expressed in terms of V_{TC} according to Eq. (3-9):

$$P_{TC} = \frac{P_O}{P_I} = \frac{V_{TC}^2 Z_O}{|Z_L|} \tag{3-9}$$

Figs. *3-5* a)-c) show examples of spectral plots of $|Z_{34IN}|$, P_{TC} and V_{TC} computed from Eq. (3-6), Eq. (3-9), and Eq. (3-8), respectively. In Figs. *3-5* a) and b) it can be seen that the closer $\mathbf{Z_L}$ is to Z_{34IN} the higher the resonant peak and the more power is available for the IC. Another point of interest is that if $\mathbf{Z_L}$ is less Z_{34IN} the bandwidth of the resonance is substantially larger than if $\mathbf{Z_L}$ is greater Z_{34IN}. From Figs. *3-5* c) it can be seen that the higher the value of $\mathbf{Z_L}$ the greater the voltage is at the terminals of the IC. The latter observation is particularly useful for the operation of the PSN. Advantage can be taken of this feature to generate the higher voltages that are required during the early stages of tuning the circuitry to the IC. Of course, the minimum power requirements (in terms of load current) of the IC establish a maximum value for Z_L as well.
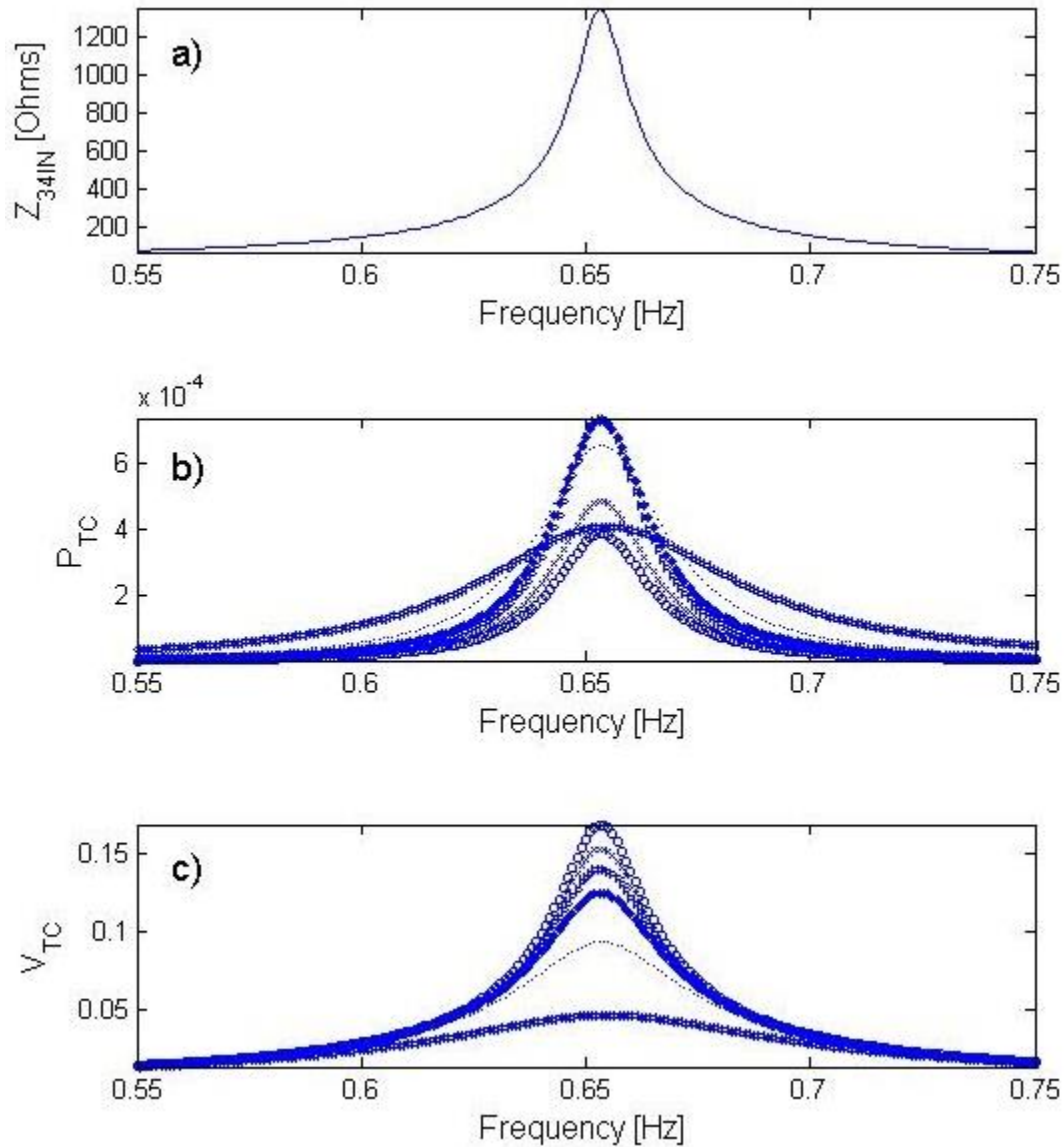
Fig. 3-5: Spectral plots showing the resonances of three computed TXC electrical characteristics: a) $|Z_{34IN}|$, b) P_{TC} computed for different load impedances, and c) $|V_{TC}|$ computed for different load impedances. In b) and c) symbols are used as following: 'o' - $Z_L= 1.5*Z_{34IN}$; 'x' - $Z_L= 1.2*Z_{34IN}$; '*' - $Z_L = 0.8*Z_{34IN}$,; '.' - $Z_L= 0.5*Z_{34IN}$; '<' - $Z_L= 0.2*Z_{34IN}$; and '>' - $Z_L= Z_{34IN}$.

An actual TXC structure has more components than the simple coupled transmission line model shown in Fig. 3-1. Reference [11] focuses on the development of a compact mathematical model for idealized TXC. This thesis is concerned with understanding the behavior of different TXC devices in real systems. There are several key components and characteristics of a real TXC system that should be defined. Table 3-1 defines these components and describes key characteristics in terms of their importance in quantifying the behavior of the TXC.

Table. 3-1: Key components and characteristics of the TXC system.

C_T $X_c = 1/jwC_T$	Tuning capacitance placed at the terminals of the TXC to induce resonance at a selected frequency, f_r. and associated reactance.
R	The resistance of the TXC leads and loop structure. This resistance has a direct contribution on the Q factor of the TXC and power loss.
L $X_L = jwL$	The inductance of the TXC loop, which along with C_T, is responsible for the resonance at f_r and associated reactance. The value of this inductance effects Q.
Q $Q = \dfrac{f_r}{BW}$ $Q = \dfrac{1}{R}\sqrt{\dfrac{L}{C}}$	Q-factor or quality factor is a measurement of the energy stored in a resonant circuit compared to the energy supplied by the generator. In this instance it reflects the overall efficiency of the TXC.
f_r $w_r = 2\pi f_r$ $w_r = \dfrac{1}{\sqrt{LC_T}}$	The resonant frequency is a design parameter that is also important in determining Q. f_r is used to distinguish different TXC structures in later sections.
BW	Band width is the measure of the -3dB fall-off points from the peak of the main resonant lobe. It is also important in determining Q. BW is also an important factor for consideration when designing resonant tuning structures, since the tuning structure has only a limited ability to change the resonant frequency.

Fig. 3-6 defines the *Q*-factor. The bandwidth, *BW*, is the difference between the two -3dB points on the curve and is given by *BW = f₁-f₂*. The Q-factor is defined in this thesis as *Q = fr/BW* for the power transfer characteristic, P_{TC}. Higher Q-factors are associated with lower total resistance in the resonant circuit. A higher Q- factor means that there is a much smaller bandwidth over which power is available at the outputs of the TXC and a lower Q-factor means that less power is available for a given frequency interval in the bandwidth. In order to provide power harvesting and telemetry functions for an IC in a PSN, the Q-factor of the TXC structure must lie within an acceptable range that depends on the ability of the IC to tune the TXC structure toward resonance. Due to variations in manufacturing of the IC, the TXC, and the bulk tuning capacitor there will be a variation in the default resonance of the TXC system. To tune the TXC system to an optimized resonant frequency, the IC will need to have a tuning

mechanism that can operate even for power levels off of resonance. The smaller the variations in manufacturing tolerances of the TXC system the higher the Q factor can be and still achieve an acceptable yield.
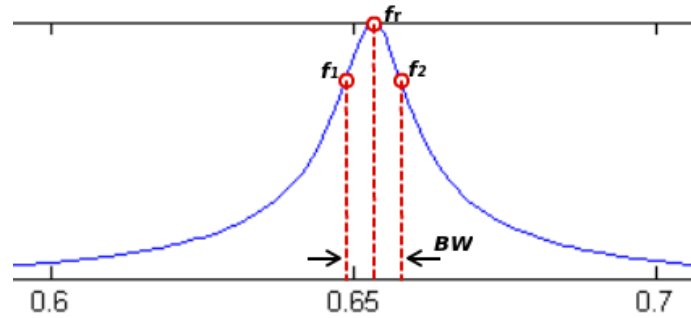
Fig. 3-6: Definition of the Q-factor. The frequency f_1 **is the** $-3dB$ **fall-off point to the left of the resonant peak,** f_2 **is the** $-3dB$ **fall-off point to the right of the resonant peak,** f_r **is the frequency of resonance, and BW is the bandwidth.**

It can easily be shown that the Q-factor can also be approximated by an expression that contains the equivalent inductance, capacitance, and resistance of a circuit. Table 3-1 lists an alternative expression,

$$Q = \frac{1}{R}\sqrt{\frac{L}{C}} \quad ,$$

(Eq. 3-10)

that is appropriate for the tank circuit shown in Fig. 3-7 a). This simple circuit includes an inductance (**L**) that could be a transformer with a finite resistance (**R**) with a shunting tuning capacitance (**C_T**). The TXC can also be approximated near resonance by the circuit shown in Fig. 3-7 b) a parallel RLC circuit where

$$R'=R(Q^2+1) \; .$$

(Eq. 3-11)

Although the influence of the coupled transmission line isn't included, the equivalent resonant behavior of the TXC is adequately represented by this simple circuit.
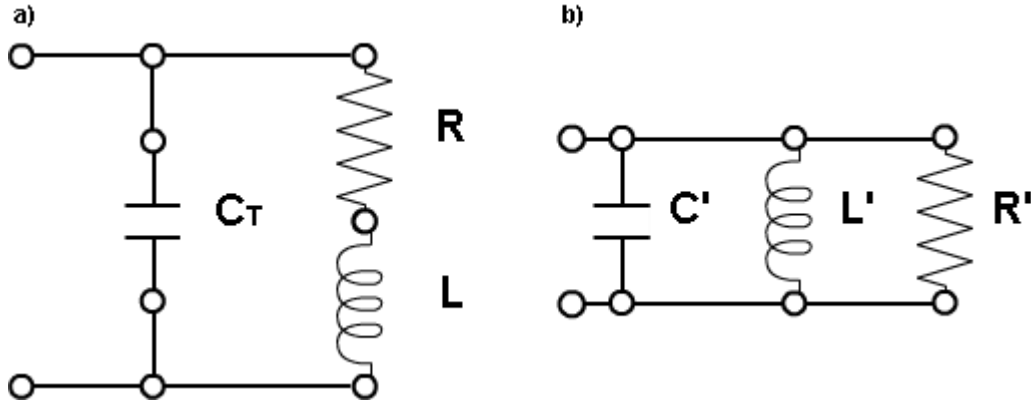
Fig. 3-7: An RL parallel C tank circuit with series L and R elements and a parallel C_T element and a parallel RLC circuit with parallel L', R', and C' elements, that are electrically equivalent to the TXC near resonance.

The TXC includes a wire loop antenna and the inductance of the equivalent tank circuit is primarily due to this wire loop. The inductance of a wire loop can be approximated by the expression given in Eq. (3-12), where x and z are the dimensions of the rectangle, a is half of the cross sectional area of the wire, and Y is a skin effect correction factor which has a value of one fourth at frequencies on the order of 1 GHz [12]:

$$L_{loop} = \frac{1}{\pi}\left(x\ln\frac{2x}{a} + z\ln\frac{2z}{a} - (x+z)(2-Y) + 2\sqrt{x^2+z^2} - x\arcsin\frac{x}{z} - z\arcsin\frac{z}{x}\right)$$

(3-12)

The equivalent tank circuit is a useful tool for analyzing the TXC. Systematic measurement of the complex frequency response of the TXC can be analyzed in terms of parameters that can then used to develop a mathematical model. For example, for a given value of C_T, using the value of L from Eq. (3-10) to approximate the inductance of the loop and a measurement of the Q-factor should enable computation of a value for R in the TXC structure.

Chapter 4 Geometric Study of the TXC

In Chapter 1 the notion of a coaxial connector with an embedded sensor platform is introduced. As discussed, the embedded TXC structure combines some of the functional features of near-field RFID structures and directional couplers. However many critical electrical and mechanical design requirements that constrain the geometry and the fabrication are unique to the TXC. Electrical and mechanical design and fabrication considerations include such things as impact of the TXC on the transmission characteristics of the coax transmission line (RF stealth factor), sensor platform material composition, assembly method, radial symmetry requirements, separation distance of the TXC loop from the coax center conductor, dimensions of the TXC loop, fabrication limitations in forming the TXC loop trace, composition of the TXC loop trace, and limitation imposed by the measurement probes. This chapter discusses design limitations on TXC devices that will fabricated for the geometric study.

Fig. 4-1 shows a schematic cross-sectional diagram of the TXC. An expanded cross-sectional view of the metal trace that forms the TXC loop is shown in the insert. The metal trace is characterized by a thickness (t) and a width (w). These dimensions are used in the TXC loop inductance calculation (see (Eq. 3-12)) to compute the cross-sectional area of the trace, $a = w*t$. The thick vertical dotted lines represent the coaxial cable outer conductor body or shield and the thin solid vertical lines represent the coaxial cable center conductor or center pin. The grey rectangles to either side of the center pin represent the TXC substrate and the rectangular loop labeled "TXC" in the diagram represents the TXC loop structure. Three dimensions characterize the TXC loop structure. These are: 1) the distance of the edge of the loop from the center of the center conductor (d), 2) the length of the side of the loop that lies along the x-axis (x), and 3) the length of the loop that lies along the z-axis (z).
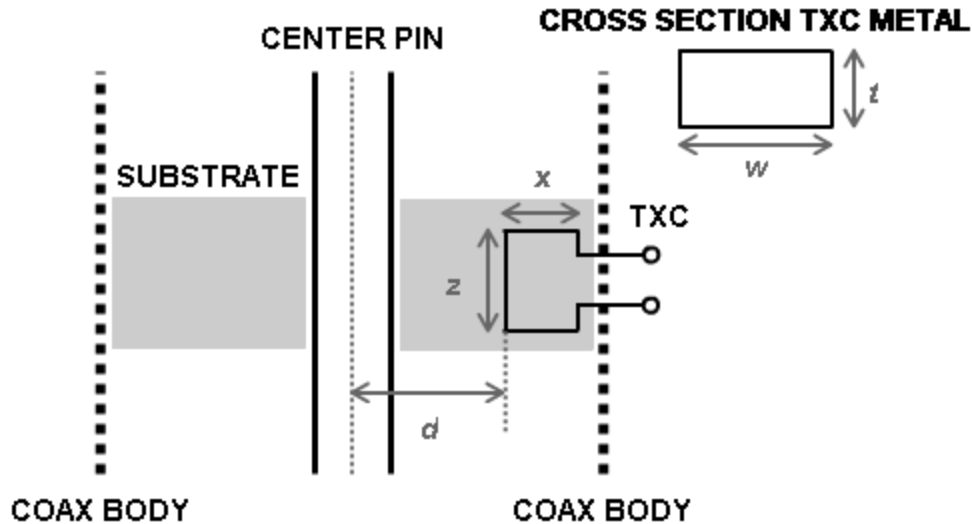
Fig. 4-1: Cross-sectional diagram of the TXC. The insert shows an expanded view of the cross section of the TXC metal trace.

It can be seen from Fig. 4-1 that there are physical limits to the dimensions d, x, w, and t. The separation distance, d is limited by the space available between the coax body and the center pin. Furthermore d must be at least a millimeter in size in order to prevent damage due to arcing between the center conductor and the loop.

Loop metal race dimensions w and t are constrained by the LDS (laser defined structuring) process used to form the metal upon the plastic substrate. The dimension w is controlled by passing a laser beam repeatedly across the substrate material. This dimension is constrained by the available flat area on the TXC substrate and by the beam width of the activating laser. The dimension t is controlled by the chemical plating process used to "grow" the metal in predefined laser-activated areas on the plastic substrate. The constraints for t include the metal or metals used in the plating process as well as the amount of time the metal is in the plating bath.

The dimensions x and z are constrained by the physical size and shape of the substrate. Limitations are placed on the attack-angle of the activating laser beam with respect to the substrate surface. These limitations are associated with obstructions that arise from the physical shape of the

substrate and from the requirement that the energy density of the projected laser beam width on the substrate surface must exceed a minimum value in order for activation to occur. The result is that metal traces cannot be placed arbitrarily close to certain edges of the substrate. Additionally, the topography of the substrate surface upon which a trace is to be formed cannot be too abrupt. Forming a metal trace on an edge requires that the edge be gently rounded. The size and shape of the substrate is not only constrained by the available space between the center pin and the coax body, it is also constrained by the necessity for structural integrity and mechanical stability of the final molded product. It should also be mentioned that RF stealth operation demands that perturbation of the coaxial transmission line be minimal. This is another reason why the TXC assembly should be as small as possible. Unfortunately, the need for minimal size, structural stability, and adequate functionality for the sensor platform components are usually conflicting requirements.

Table 4-1 outlines the physical limits on the various TXC dimensions (see Figure 4.1) for devices fabricated for the geometric study. Many of these constraints arise from the need to maintain coaxial cable standards. For example, it was necessary to fabricate a DIN 7/16 inline coaxial connector with a specialized test port for devices in this study. This is discussed further in Chapter 5.

Table 4-1: Physical limits on the TXC test device dimensions

Parameter	Max	Min
x	4 mm	1 mm
z	5 mm	1 mm
d	7 mm	4 mm
t	.05 mm	.01 mm
w	.5 mm	.25 mm

Geometric features of the TXC that were varied in the study include aspect ratio, metal width, separation distance, and loop area (see Fig. 4-1). Aspect ratio is defined as $r = x/z$ and loop area is given by $A = x*z$.

The "Control" loop is defined to be a loop which has the following dimensions: $x = 2$ mm, $z = 2$ mm, $d = 6$ mm, and $w = 0.25$ mm. The Control loop has an aspect ratio of $r = 1$ and an area $A = 4$ mm^2. The loop structures shown in Fig. 4-2 illustrate several geometric variations. For reference the Control loop is shown as dashed white lines superimposed on each loop structure. The top left "Aspect Ratio" loop shows an aspect ratio other than 1. The top right "Loop Area" shows a loop with an area smaller than the loop area of the Control loop. The bottom left "Width" shows a loop with a trace width, w, greater than that of the Control loop. The bottom right "Sep. Distance" shows a loop similar to the Control loop with a separation distance from the center conductor, d, greater than that of the Control loop.
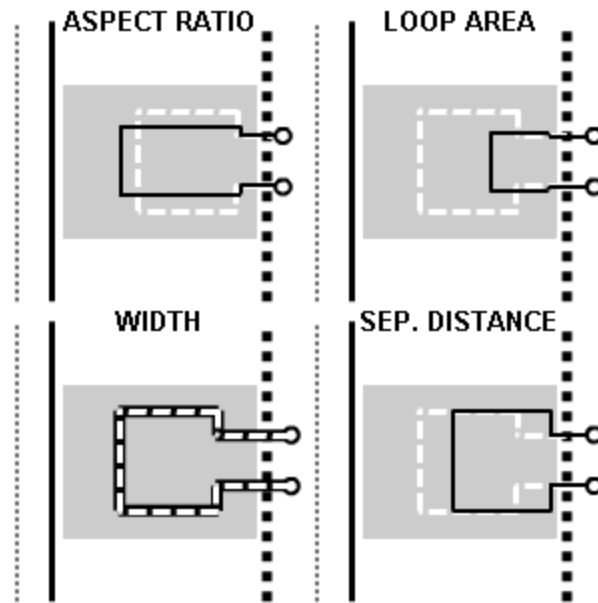

Fig. 4-2: Four types of geometric variations of the TXC loop structure are shown in solid black lines. The Control loop in white dashed lines is provided in reference.

The geometric variations outlined in Fig. 4-2 are the primary set of physical variables that were adjusted in both experimental and HFSS simulation tests.

Chapter 5 Test Fixture and Procedure

The goal of performing a geometric study is to relate physically adjustable parameters of the TXC system to electrical characteristics. There are several steps in designing, fabricating, assembling, and finally testing TXC devices. The main components of the TXC test system are the TXC test device, the TXC test fixture, and a Vector Network Analyzer (VNA) with precision cables, calibration kit, and adapters.

Fabrication of TXC test devices begins with the TXC sensor platform substrate which is a plastic material with embedded metal catalysts and a small amount of glass filler for better mold performance. The TXC substrate is made by injection molding the plastic into a steel mold. The TXC substrate is designed to support several sensor structures, IC's with telecommunications and data processing capabilities, and the TXC itself. These functions require surface metallization for sensor transducers, IC interconnect, and the TXC structure. A process called laser defined structuring (LDS) is used to accomplish this task [14]. The LDS process uses a laser to activate the metal catalysts inside of the plastic material which is then bathed in a metal ion rich liquid to grow metal on the surface of the substrate. The metallization used in the TXC system includes a thicker undercoating of copper with a thinner surface coating of silver. Fig. 5-1 is an image of a molded TXC sensor platform substrate showing the surface traces associated with the TXC loop structure.
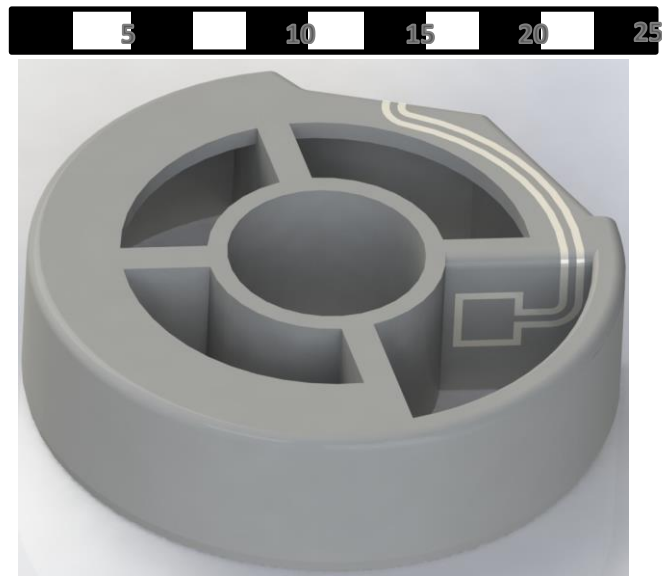
Fig. 5-1: A 3D rendering of a molded TXC substrate and TXC structure. The scale is in millimeters.

The TXC test fixture is shown as an exploded view with each individual part labeled in Fig. 5-2. A custom brass DIN 7/16 inline adapter was constructed with a plug end on one side and a jack end on the other. The inline adapter also includes dielectric inserts used to maintain the separation between the center pin and the coaxial body of the adapter. The TXC substrate is press-fit into the coaxial adapter body such that the probe portal is aligned with pads on the TXC structure to allow the coaxial probes to make electrical connection with the pads. The TXC test fixture parts are press-fit into place using an arbor press with attachments designed to prevent damage to the components during assembly. After each component is press-fit into the adapter body and the coaxial probes are soldered into place on the PCB test probe fixture, the PCB test probe fixture is attached to the inline test adapter using brass screws.

The next step in the assembly of the TXC test fixture is press-fitting the ground sleeve and dielectric insert into the inline test adapter. The ground sleeve is a standard coaxial connector ground connection part and the dielectric insert is a polyethylene part that is necessary to keep the center pin of the coaxial system in place. The DIN 7/16 inline test adapter body is the ground of the coaxial test fixture. The PCB test probe fixture is used to position the coaxial pogo probes precisely with respect to the pads on the TXC structure. As mentioned previously, the probe portal allows the coaxial pogo-pin

probes to enter the coaxial adapter body and connect with the TXC structure pads. An image of the

assembled TXC test fixture is shown in Fig. 5-3.
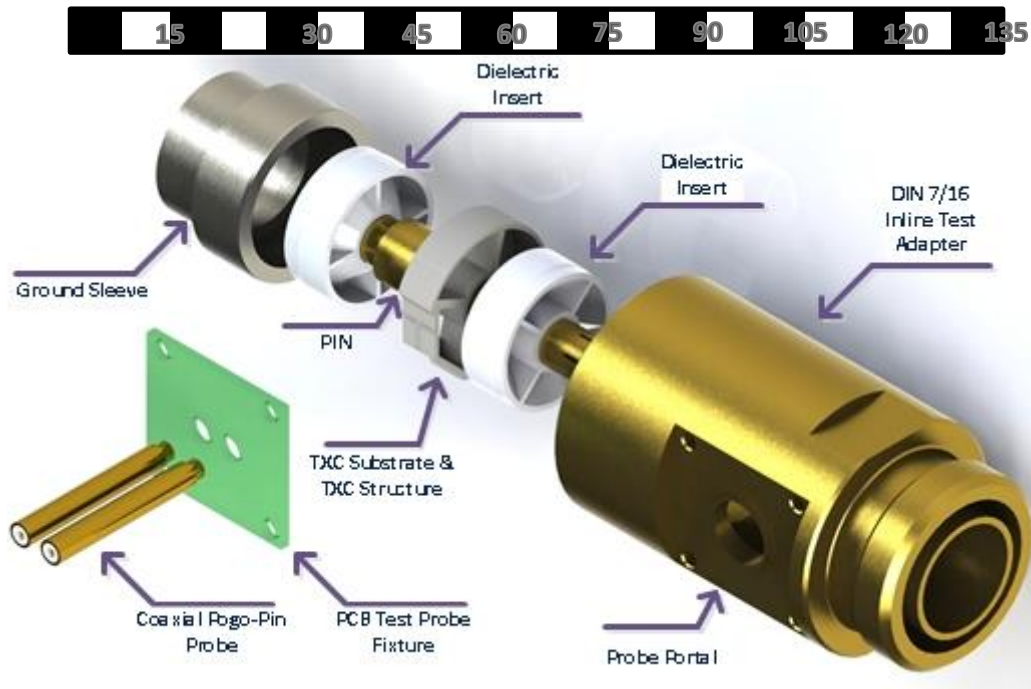
Fig. 5-2: 3D rendering of an exploded view of the components of the TXC test fixture. The scale is in millimeters.

Three of the four electrical ports of the system can be seen in Fig. 5-3. The port corresponding to

the connector plug is visible at one end of the DIN 7/16 inline adapter body and two ports are at the ends

of the coaxial pogo pin probes which are supported by the PCB probe platform. Note that the actual

connector plug end is threaded (see Fig. 5-4). The version shown in Fig. 5-3 was used in HFSS modeling

and was rendered without a thread for the sake of simplicity.
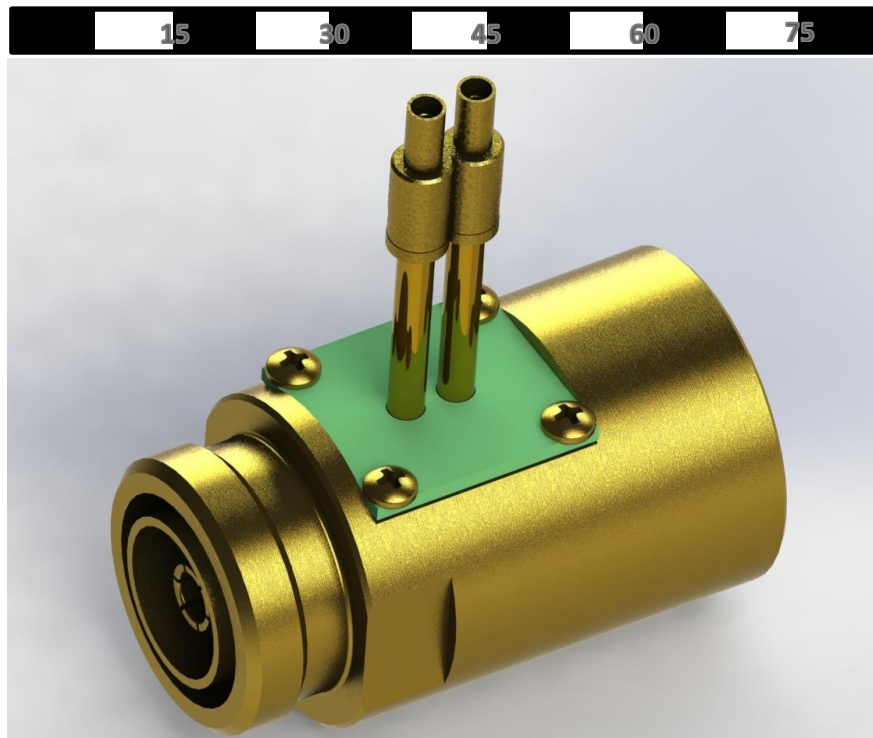
Fig. 5-3: A 3D rendering of an assembled TXC test fixture with probe connections.

Images of the unassembled and assembled test-fixture are presented in Fig. 5-4. Shown in this figure are the dielectric inserts, the molded TXC platform, the coaxial center pin, the ground sleeve between the two inline adapters, and the coaxial pogo pin probes/fixture with screws. The two inline adapters are featured at the top of the page. Fig. 5-4 also shows the special positioning tool that was made to assemble the test-fixture.
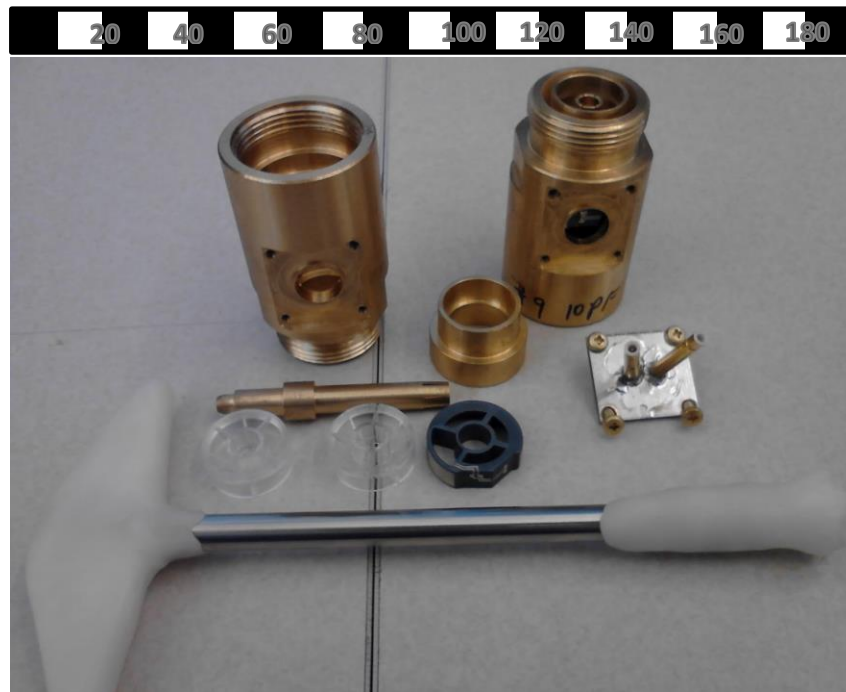
Fig. 5-4: An unassembled test fixture and an assembled test fixture with a TXC platform and TXC structure test ports.

The VNA was an Agilent series E5071C including one phase stable precision N-type jack-to-DIN 7/16 plug, one phase stable precision N-type jack-to-DIN 7/16 jack, a DIN 7/16 jack-to-3.5 mm jack, a DIN 7/16 plug-to-3.5 mm jack, two 3.5 mm plug-to-SMB plug, and two SMB plug-plug cables. The VNA test system also included a DIN 7/16 calibration kit with open, short, and fixed load. Fig. 5-5 shows an inline adapter test fixture with VNA cables attached. Two SMB connectors are attached to the pogo pin probes and the two DIN 7/16 connectors are attached to the inline adapter. Fig. 5-6 shows an image of the entire test system used to make the measurements including the cable and adapter components.
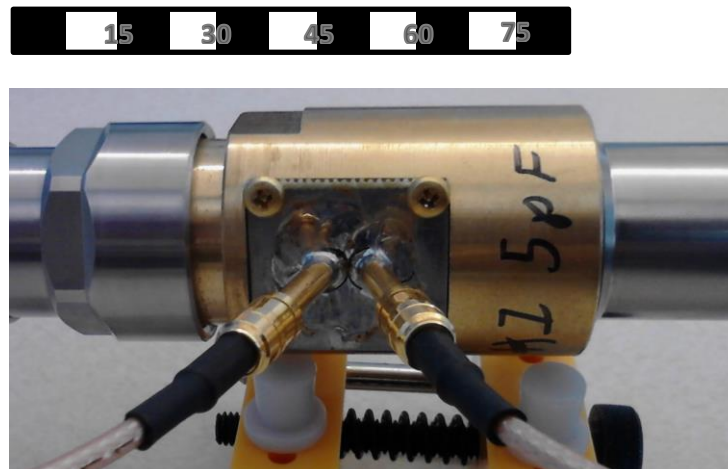
Fig. 5-5: The assembled TXC test fixture with interconnect cables from the VNA.

Fig. 5-6: The TXC test structure attached to the VNA with precision phase stable cables.

It should be noted that the Agilent series E5071C VNA used in these experiments is a two-port instrument. In order to accomplish four-port measurements, a stepped testing procedure had to be employed. Since this VNA conforms to 50 ohm standards, 50 ohm loads can be used to terminate ports without VNA test cables attached. In this way all of the S-parameters can be measured and recorded.

Recall from Chapter 3 that geometric considerations led to constraints on aspect ratio, separation distance, surface area, and lead thickness. Fig. 5-7 illustrates the seven TXC test structures used in this study with a label indicating how each structure deviates from the Control loop. Table 5-1 contains the same information with precise details as to the construction of each TXC test structure.

Table 5-1: Specification of the geometric features of the seven TXC test structures.

Test #	Aspect Ratio	Dimensions	Trace Thickness	Sep. Distance
1	1:1	2mm x 2mm	.3 mm	6mm
2	1:2	1.4mm x 2.8mm	.3 mm	6mm
3	2:1	2.8mm x 1.4mm	.3 mm	5.6mm
4	1:1	2mm x 2mm	.5 mm	6mm
5	1:1	1mm x 1mm	.3 mm	6mm
6	1:1	1mm x 1mm	.3 mm	5mm
7	1:1	1mm x 1mm	.3 mm	7mm
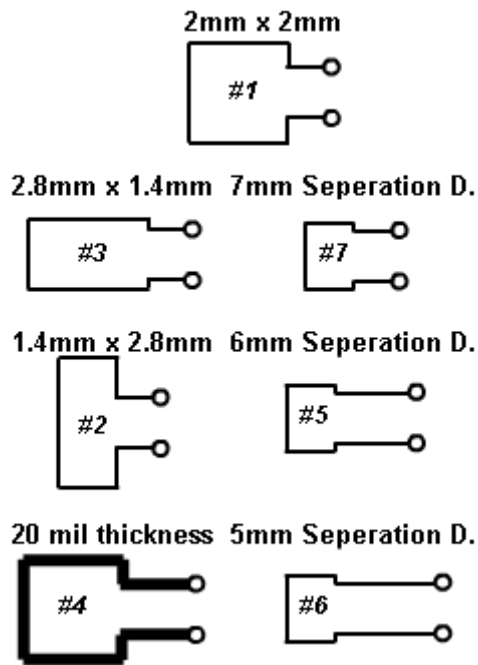
Fig. 5-7: Pictorial representation of the seven test structures described in detail in Table 5-1.

The TXC test structures described in Table 5-1 and depicted in Fig. 5-7 were fabricated, assembled, and tested according to the process detailed earlier in this chapter.

HFSS Simulation

Advantages of using a simulator for characterizing the TXC system include the low cost of repetitive testing, the increase in consistency between tests, the ability to test rapidly a variety of

structures, the ability for computer automation to simplify the work, and the ease of modifying and improving the test system itself. The disadvantage in using a simulator, especially for RF simulations, is the need to develop an initial fitting of the simulator. The process of fitting involves adjusting simulator parameters in order to obtain electrical characteristics that accurately represent those of the real system.

The simulation data for the TXC geometric study was generated using the High Frequency Structure Simulator (HFSS) from Ansoft Corporation. HFSS is a finite element radio frequency simulation software package with a built-in 3D CAD interface and the ability to import 3D CAD models from other software. The 3D CAD models used to create the TXC test fixture and TXC test structures is imported into the HFSS software with minimum modifications. An image of the 3D CAD modeler in HFSS of the TXC test fixture is displayed in Fig. 5-8.

The brass outer body is a combination of the grounded shield of the DIN 7/16 inline adapter body, the pogo pin probe ground shielding, and the PCB test probe fixture. The coaxial opening at Port 2 (connector plug end) and the coaxial openings at Ports 3 and 4 (pogo pin probes) are shaded to designate the measurement ports that HFSS uses as the boundary to measure and compute the simulation data.
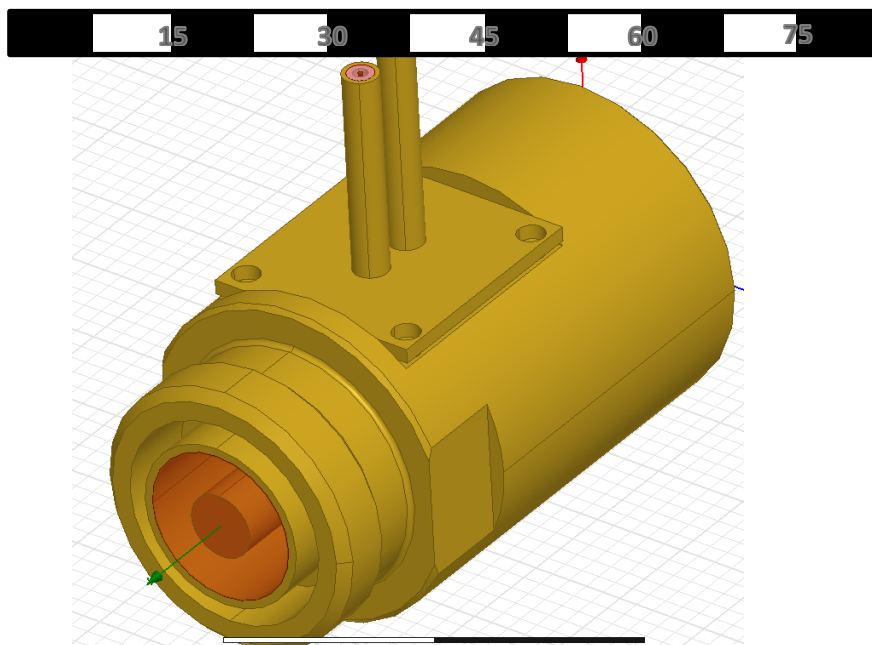
Fig. 5-8: An image of the 3D CAD model produced by HFSS and used in the simulator for the high frequency simulations.

The main difference between the HFSS TXC test fixture and the experimental TXC test fixture is that the HFSS test fixture has "united" metal connections. This means that at every metal interface the conductors are considered completely and seamlessly merged in the simulator. This assumption means that any contact resistance or capacitive parasitics that may be present in the experimental test fixture are ignored in the HFSS simulation.

As mentioned previously in Chapter 4, experimental TXC test structures include metallization that was formed by laser-activation of a catalyst on the surface of the substrate followed by growth of metal in a bath. Obviously this process isn't well-characterized in terms of the conductor properties and may differ from any of the conductor properties for materials listed in the HFSS library. In the HFSS simulations .01 millimeter thick copper was used as the conductor. A thinner than expected "grown" conductor could account for unexpected values of loop resistance as well as increased capacitive and inductive parasitics.

Finally, it should be noted that several minor modifications in the mechanical design were made to allow for simulation matrix mesh convergence. These modifications did not significantly alter the RF behavior of the TXC test fixture. An example of such a modification was that the center conductor in the simulator was made without chamfers at the ends of the pins. The chamfers physically are used to make a cylindrical connection when inserting the connector into the mating center pin of another connector.

Chapter 6 Geometric Study Results

As discussed in Chapter 5, Test Structure 1 was used as a control in the TXC geometric study. Test Structure 1 is ideal for this designation since all the other structures are variants of this basic structure. Test Structures 2 and 3 have different aspect ratios, although they have the same overall loop surface area as Test Structure 1. Test 4 has a much thicker trace width than the Control loop. Table 5-1 and Fig. 5-7 give detailed information about the differences between the seven test structures. This chapter reports the results of RF measurements and HFSS simulations of the electrical characteristics of these seven test structures.

Results of RF Measurements and HFSS Simulations of S-parameters

Bode plots of the six independent S-parameters for the experimental results and HFSS simulations of TXC Test Structure 1 with a 10 pF tuning capacitor are shown in Fig. 6-1 (magnitude) and Fig. 6-2 (phase). The HFSS simulation results are fitted although it should be noted that the S-parameter responses for fitted and unfitted HFSS data are nearly indistinguishable. Z-parameters were obtained from this data using Eq. (3-5) and $/V_{TC}/$, P_{TC}, and Z_{34IN} were then calculated from the Z-parameters using Eq. (3-8), Eq. (3-9), and Eq. (3-6) respectively. Fig. 6-3 shows plots of $|Z_{34IN}|$ for experimental and simulation data as an example. Note that $|Z_{34IN}|$ exhibits two distinct peaks. The frequency of resonance (f_r) is defined as the frequency at which the first peak occurs. This frequency corresponds to the resonant peaks of both $|S_{13}|$ and $|S_{14}|$ (see Fig. 6-1) The occurrence of two peaks in $|Z_{34IN}|$ will be discussed more in Chapter 7. Fig. 6-4 shows plots of Test Structure 1 with tuning capacitors of 10 pF and 5pF as a demonstration of the effects of C_T on the resonant frequency.
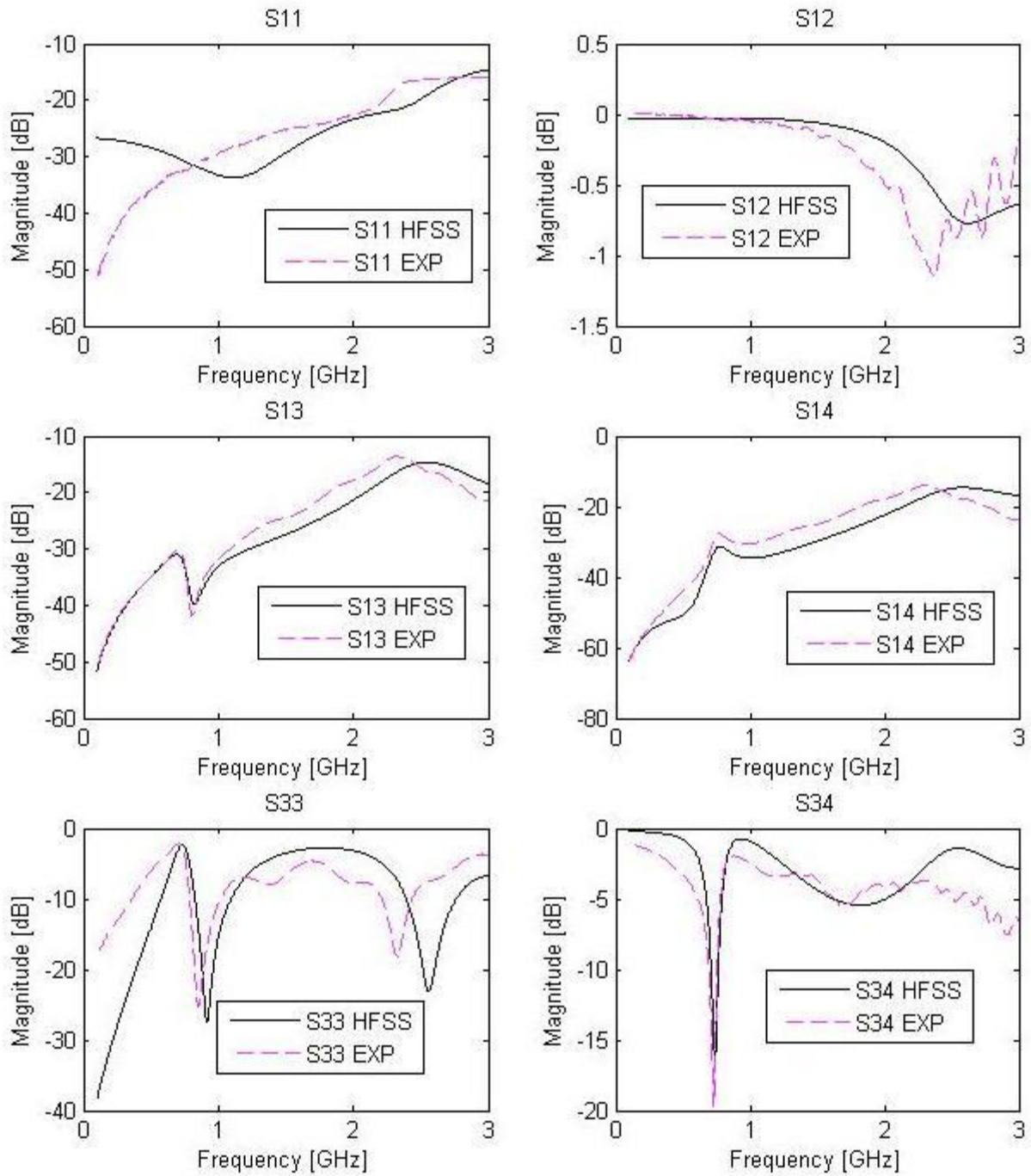
Fig. 6-1: Spectral plots of the magnitude in dB of the six independent S-parameters of TXC Test Structure 1 with $C_T = 10$ pF for experimental and HFSS data.
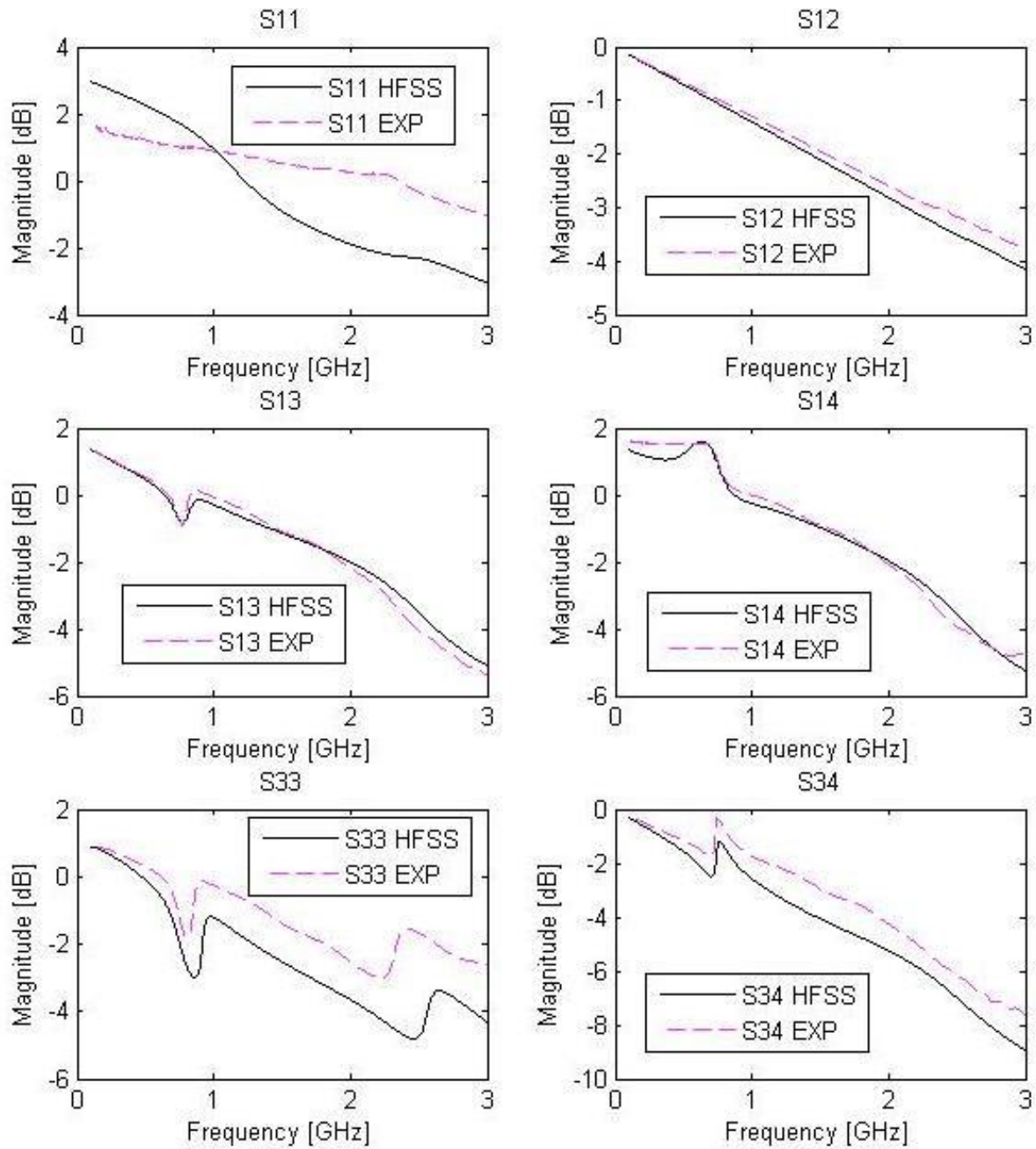
Fig. 6-2: Spectral phase plots of the S-parameter data shown in Fig. 6-1.
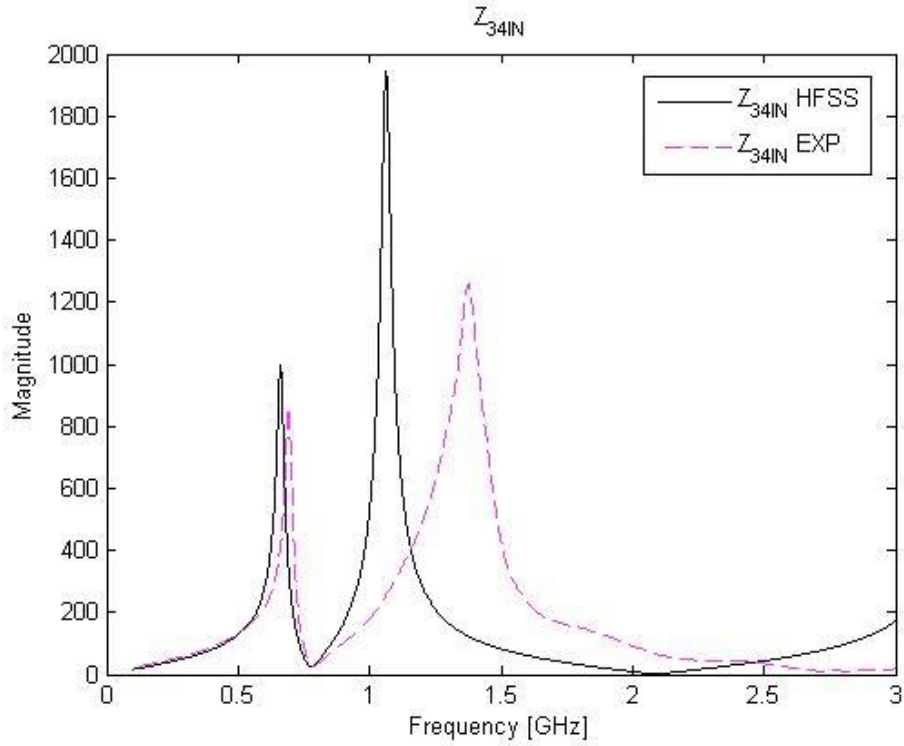
Fig. 6-3: The frequency response of Z_{34IN} for TXC Test Structure 1 with C_T = 10 pF showing experimental and fitted simulation results.
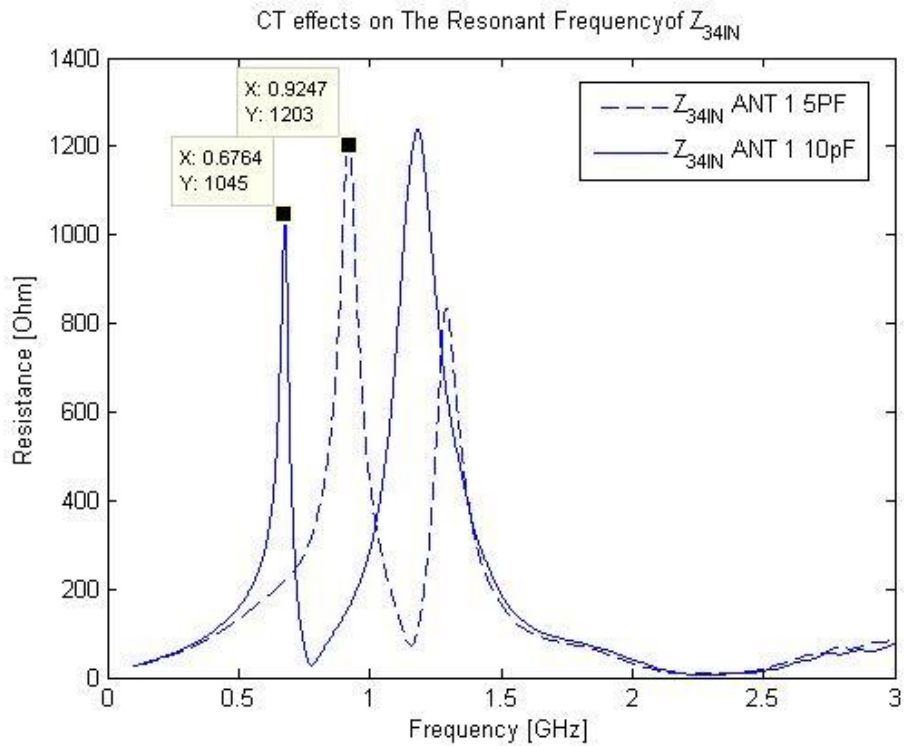
Fig. 6-4: The $|Z_{34IN}|$ frequency response of Test Structure 1 with a 5 pF and a 10 pF tuning capacitance.

TXC Performance Factors

Computed quantities such as Q-factor, $|V_{TC}|$, P_{TC}, $|Z_{34IN}|$ at resonance, and f_r were defined previously in Chapter 2. These quantities are measures of how well a given test structure performs as a transmission line coupler, and as such, they permit a quantitative comparison of the test structures.

Values of experimentally derived Q-factor, $|V_{TC}|$, P_{TC}, $|Z_{34IN}|$ at resonance, and f_r are shown plotted in Fig. 6-5 and listed in Table 6-1 for all seven test structures with a 10pF tuning capacitor. Also shown plotted Fig. 6-5 and listed Table 6-1 is the Coupling Factor (CF). CF is another RF characteristic that is used to assess the performance of a test structure. It is a measure of the strength of the coupling between the test structure and the coaxial line and is defined as the measured ratio of powers at Ports 3 and 1 measured in dB. This factor is useful in the optimization of the coupling characteristics of the TXC. This includes maximizing coupling at the resonant frequency and minimizing coupling at all other frequencies. P_{TC}, $|V_{TC}|$, $|Z_{34IN}|$, and CF data points are taken at the resonant frequency. All quantities are plotted on the y-axis with the sample number on the x-axis.

Comparison of Performance Factors derived from HFSS simulations with those derived from experimental data are presented in Fig. 6-6. HFSS Performance Factors are listed in Table 6-2. "Unfitted" HFSS simulations, referred to in the caption of Fig. 6-6, were obtained using HFSS library parameters with no adjustment. The reader may notice several discrepancies between TXC Performance Factors derived from experimental data and HFSS simulations. These discrepancies will be addressed in Chapter 7.
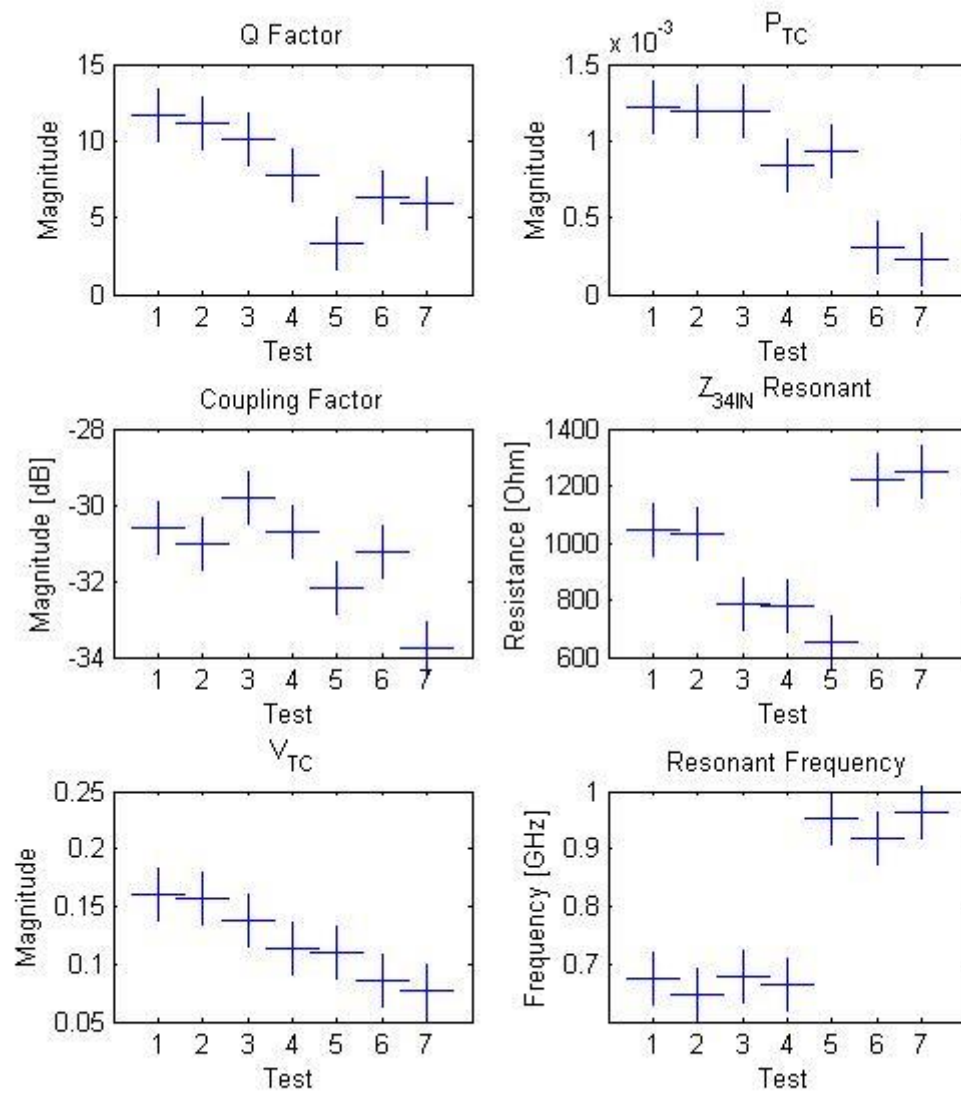
Fig. 6-5: The TXC Performance Factors for the seven experimental test structures with $C_T = 10$ pF.

Table 6-1: Tabulation of the data displayed in Fig. 6-5.

	1	2	3	4	5	6	7
$|Z_{34IN}|$ (Ohms)	1.0451e3	1.0303e3	788.388	776.1936	650.8091	1.2203e3	1.2522e3
Q Factor	11.6616	11.1304	10.1128	7.8122	3.3665	6.2614	5.9682
V_{TC}	0.1596	0.1566	0.1373	0.1143	0.1101	0.0861	0.0762
P_{TC}	0.0012	0.0012	0.0012	8.4090e-4	9.3118e-4	3.0408e-4	2.3190e-4
Coupling Factor (dB)	-30.5853	-31.0054	-29.799	-30.7159	-32.1695	-31.2234	-33.7736
f_r (GHz)	0.6764	0.6456	0.6782	0.6655	0.9519	0.9193	0.9628
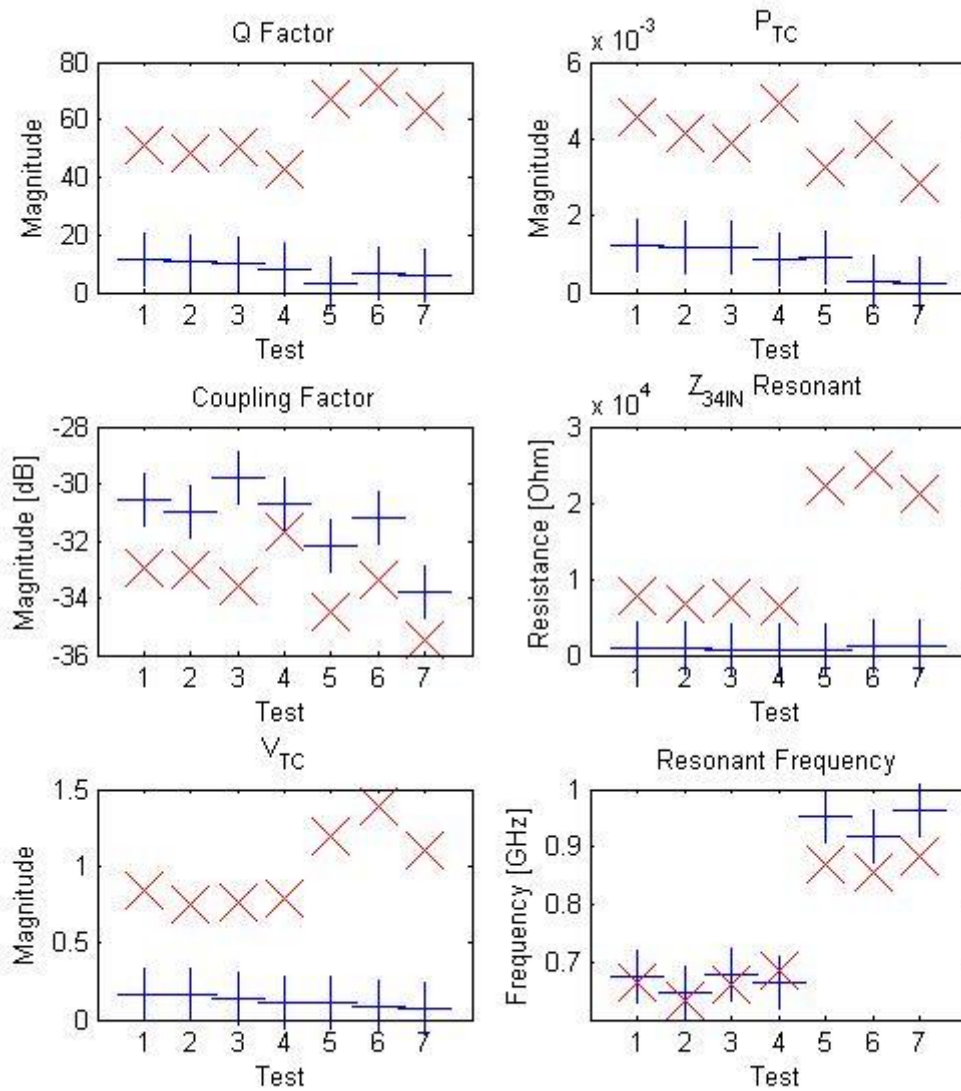
Fig. 6-6: **TXC Performance Factors for the seven experimental test structures and the unfitted HFSS simulation results. The symbol '+' represents experimental data from Fig. 6-5 and the symbol 'x' represents HFSS-derived data.**

Table #6-2: Tabulation of the HFSS data displayed in Figure 6-6.

	1	2	3	4	5	6	7
$|Z_{34IN}|$ (Ohms)	7.8008e3	6.8230e3	7.4405e3	6.3284e3	2.2106e4	2.4239e4	2.1274e4
Q Factor	51.2308	48.6923	50.7692	42.7500	67.0000	71.2500	63.0000
$|V_{TC}|$	0.8431	0.7513	0.7601	0.7884	1.1987	1.3867	1.0979
P_{TC}	0.0046	0.0041	0.0039	0.0049	0.0033	0.0040	0.0028
Coupling Factor (dB)	-32.9627	-33.0008	-33.6078	-31.6576	-34.4567	-33.3342	-35.4410
f_r (GHz)	0.6660	0.6330	0.6600	0.6840	0.8710	0.8550	0.8820

Chapter 7 Analysis of the Geometric Study

Results obtained in the geometric study for the Port 3-Port 4 terminal impedance, resonant value of $|Z_{34IN}|$, Q-factor, $|V_{TC}|$, P_{TC}, coupling factor, and resonant frequency are discussed in this chapter. Significant differences can be observed between experimental and HFSS data for the Q-Factor, P_{TC}, $|V_{TC}|$, and resonant value of $|Z_{34IN}|$ shown in Fig. 6-6. A possible explanation for these discrepancies is the fact that the HFSS data in this figure is unfitted. Fitting refers to the process of using experimental data to adjust HFSS materials properties (see Chapter 5). A fitting study was carried out for the Control loop (Test Structure 1) and the results are also discussed in this chapter. The six performance factors listed above are discussed below followed by a discussion of the results of the fitting study.

Port 3-Port 4 Terminal Impedance

Fig. 6-3 shows the frequency response of $|Z_{34IN}|$ obtained from experiment and HFSS simulation. Two resonances can clearly be seen in both the cases. Multiple resonances in terminal impedance have also been reported in the literature for similar structures [13]. On the other hand, it is interesting to note that only a single resonant peak was reported for the TXC studied in [11]. However, it should be noted further that the TXC studied in [11] is a highly idealized version of the ones in the present study. Multiple resonances in the terminal impedance are presumably due to the effects of so many capacitances and inductances in actual TXC test structures that were not included in the idealized TXC. The so-called "primary" resonance observed in the test structures in this study seems to correspond to the single resonance reported in [11]. Further analysis and testing is necessary to determine the precise source of each resonance.

Returning once again to Fig. 6-3, the "primary" resonance is defined to be the one that occurs at the lower frequency and corresponds with the resonant behavior observed in the CF, the PSN power tone, and the S-parameters. The "secondary" resonance appears only in the terminal impedance and does not seem to

be accompanied by an increase in CF.   It can be seen from Figs. 6-4, 6-5, and 6-6 that the magnitude of $|Z_{34IN}|$ at the primary resonance appears to vary with the physical geometry of the structure and with C_T.

Resonance Value of $|Z_{34IN}|$

The experimental data in Fig. 6-5 for the resonant value of $|Z_{34IN}|$ does not seem to show a strong correlation with structure geometry, although there may be a weak correlation between loop size and this performance factor. Test structures with smaller loop areas show about 25% larger $|Z_{34IN}|$ at resonance compared to test structures with larger loop areas. Note that the experimental value of $|Z_{34IN}|$ at resonance for Test Structure 5 appears to be unusually low. It is believed that this is an artifact due to the frequency sampling interval used in experimental measurements. Resolution of the experimental sampling was much lower than that used in the HFSS simulations. Because of the relatively high Q of the TXC structures, the peak values of $|Z_{34IN}|$ could be more accurately determined for the HFSS simulations compared to experiment.

HFSS simulations shown in Fig. 6-6 suggest that loops with the larger values of x and z have lower resonant values of $|Z_{34IN}|$ while those with the smallest values of x and z have larger values of this performance factor. This is in agreement with the experimental data. The resonant value of $|Z_{34IN}|$ for test structures with smaller loop areas is about three times larger than that for test structures with larger loop areas according to the HFSS simulation.

Q-Factor

The data shown in Fig. 6-5 seems to indicate that the Q-factor, like the value of $|Z_{34IN}|$ at resonance, does not seem to be sensitive to variations in the aspect ratio (Test Structures 1, 2, and 3) or to separation of the loop from the center pin (Test Structures 5, 6, and 7). On the other hand, text structures with smaller loop areas (Test Structures 5, 6, and 7) seem to have slightly lower Q-factors compared to those with larger loop areas (Test Structures 1, 2, 3, and 4). Furthermore, the Q-factor for Test Structure 5 appears to be anomalously low which could relate to the low value measured for $|Z_{34IN}|$ at resonance mentioned previously. Note that Test Structure 4, which has thicker trace leads, has a much lower Q-factor than similarly sized TXC structures.

Q-Factor responses determined from HFSS simulations (Fig. 6-6) also indicate insensitivity to aspect ratio, separation distance, and trace thickness. However HFSS simulations show that the Q-Factor follows the trend seen in $|Z_{34IN}|$ at resonance; namely test structures with smaller loop areas have larger Q-Factors while those with larger loop areas have smaller Q-Factors. This appears to be opposite of what is seen experimentally for the Q-Factor. Here again, issues associated with the experimental sampling interval may result in measured values of the Q-factor that are smaller than expected.

It has been shown in Chapter 3 the effective resistance of the TXC tank circuit at resonance is (Q^2 +1) times the actual resistance of the inductor in the tank circuit. Therefore it is consistent that an increase in Q-factor for the TXC structures with smaller loop area should be accompanied by an increase in $|Z_{34IN}|$ at resonance for these same TXC structures.

Voltage Transfer Characteristic, V_{TC}

The experimental results in Figure 6-5 indicate that TXC structures with smaller (larger) loop surface areas tend to have a smaller (larger) $|V_{TC}|$. Test Structure 4 also has a smaller $|V_{TC}|$ response than test structures of similar dimensions. Test Structure 4 has a larger trace thickness which implies a lower loop resistance. The lower TXC loop resistance may lead to a lower resonant output impedance and a lower voltage at the output of the test structure. Test Structures 1, 2, and 3 all have similar $|V_{TC}|$ responses which imply that aspect ratio variations have a limited effect on the $|V_{TC}|$ response.

According to Fig. 6-6, computations of $|V_{TC}|$ based on HFSS simulations also indicate that $|V_{TC}|$ is insensitive to aspect ratio. However the TXC test structures with the smaller loop surface area show a larger $|V_{TC}|$ compared to test structures with larger loop surface area which is the opposite results observed experimentally. In fact, the variation of $|V_{TC}|$ with surface loop area is similar to that seen for $|Z_{34IN}|$ at resonance for computations based on HFSS simulations.

Power Transfer Characteristic, P_{TC}

It can be seen from Figs. 6-5 and 6-6, that the P_{TC} response of the test structures generally resembles the P_{TC} response of corresponding structures for HFSS simulations. The exception to this is Test Structure 4. In this case the value of P_{TC} determined from HFSS simulations is marginally greater than other structures of similar loop area, which was not seen in the experimental data.

It will be noted in Fig. 6-6 that the P_{TC} dependence on test structure geometry does not track $/V_{TC}/$ dependence for HFSS simulations. From Eq. 3-9, it is known that P_{TC} is proportional to $|V_{TC}|^2$ and inversely proportional to $|Z_L|$. Furthermore $|Z_{34IN}|$ is equal to $|Z_L|$ when the TXC is impedance matched to the load. In addition, the increase of $|Z_{34IN}|$ at resonance with decreasing loop surface area for the HFSS simulated data is much larger than it is for $|V_{TC}|$. The result is that the increase in $|V_{TC}|^2$ is cancelled by the increase in $|Z_{34IN}|$ and no increase in P_{TC} is observed for HFSS simulations.

Coupling Factor, CF

It can be seen from Fig. 6-6 that the experimental CF data seems to track the CF computed from HFSS simulations with the HFSS simulations showing a slightly weaker CF than the corresponding experimental structures. Evidently this discrepancy is due to an underestimation of the electric and magnetic coupling strength in the HFSS simulations, which may have resulted from parasitic capacitances and inductances that exists in TXC test structures but are not included in the HFSS simulations. CF seems to be lower for greater separation distance and for smaller loop surface area, although Test Fixture 6 does not conform to this trend. The aspect ratio and trace width seem to have little effect on the coupling factor with the exception of Test Structure 3.

The Coupling Factor was found to increase gradually with frequency for all test structures.

Resonant Frequency, f_r:

According to Fig. 6-6, the frequency of resonance determined from the experimental data agrees with the HFSS simulations, although HFSS simulations generally show a slightly lower resonant frequency. Both results indicate that f_r is insensitive to aspect ratio, trace width and separation distance; however, both results show an increase in f_r with decreased loop surface area.

It is well-known that the resonant frequency is related to the tank circuit inductance and capacitance:

$$f_r = \frac{1}{\sqrt{LC_T}}$$

(Eq. 7-1)

(see Table 3-1). Since in most cases the TXC test structures all use the same value of high precision tuning capacitance, the variations observed in resonant frequency must be due to variations from structure to structure in the self-inductance of the metallic loop or mutual inductance between the loop and the center conductor. It is expected that the self-inductance of the test structures should be more sensitive to the loop surface area whereas the mutual inductance should be more sensitive to the separation distance. Furthermore, the mutual inductance should act in parallel with the self-inductance. On the other hand, the

mutual inductance is typically more than an order of magnitude smaller than the self-inductance. It is therefore expected that the loop area should play a dominant role in the determination of f_r compared to the separation distance. As a check, Eq. 3-10 was used to compute the loop self-inductance for all seven TXC test structures. The results are presented in Table 7-1. A larger self-inductance implies a lower resonant frequency which means that the results in this table are consistent experimental and HFSS simulation results.

Table 7-1: Loop self-inductances (nH) for the seven test structures calculated using Eq. (3-10).

Test 1	Test 2	Test 3	Test 4	Test 5	Test 6	Test 7
5.69	7.02	7.02	5.28	2.28	2.28	2.28

Fig. 6-4 shows the effects of varying C_T from 10pF to 5pF in Test Structure 1. The observed change in the resonant frequency is consistent with the relationship in Eq. (7-1).

In concern to design specifications for resonant frequency, power, voltage, and output impedance the TXC structures presented in this study, though not specifically designed to optimize for these specifications, the structures were very close to meeting these specifications. The structure that most accurately met the specifications is test 1 with the exception of resonant frequency. Table 7-2 compares the specifications with the performance of test 1.

Table 7-2: Test 1 performance compared to desired TXC specifications.

TEST 1	P_{TC}	$|V_{TC}|$	$|Z_{34IN}|$	CF (dB)	f_r (GHz)
EXP	0.0012	0.1596	1045.1	-30.5853	0.6764
SPEC.	0.0010	0.002	1000	-30	0.8465

With the information from this study an appropriate tuning capacitor could be found to place the resonance of the structures within an acceptable range for refined tuning from the PSN IC.

Fitting Study

The accuracy of HFSS simulations of TXC test structures depends on how accurately the materials properties are known. In particular the electrical conductivity of the LDS-based trace metallization and the dielectric constant of the specialized substrate plastic that is used in the LDS process must be known to obtain realistic simulation results. For example, an overestimation of the trace conductance would cause overestimations of $|Z_{34IN}|$, Q-factor, $|V_{TC/}|$, and P_{TC}. All of these features were in fact observed. Accordingly, it was hypothesized that the agreement between HFSS simulations and experimental data could be significantly improved by "calibrating" the HFSS simulation by adjusting the trace conductivity to obtain a match with experimental data. On the other hand, it should he emphasized that calibrating the HFSS simulation does not overcome limitations due to insufficient experimental sampling.

In order to test this hypothesis "unfitted" HFSS simulations were carried out using copper as a trace conductor material with properties taken from the HFSS library. Trace conductors were formed on experimental test structures using plated metal developed in a bath system. Electrical measurements were then taken on these test structures, and an estimate for a correction factor was obtained by comparing $|Z_{34IN}|$ at resonance for the HFSS simulations and for the experimental data. The HFSS simulations were then repeated after adjustments to material constants were made based on the experimental measurements.

Table 7-3 lists the results of the HFSS simulations after fitting compared to the experimental results for Test Structure 1 and C_T= 10 pF. The table clearly shows a substantial improvement in the agreement between the performance factors computed from HFSS simulation and those computed from experimental results when the fitting process is applied to the HFSS simulation. It should be cautioned that these results are from a preliminary study, and that the fitting of the simulator is only as accurate as the experimental data used in the process. The Q-factor of the TXC structures could be much higher than that of the experimental data. An iterative approach of experimental and simulation refinement would be appropriate to generate the best results.

Table 7-3: Electrical performance factors computed from experiment, fitted HFSS simulation, and unfitted HFSS simulation for Test Structure 1 with C_T= 10 pF.

TEST 1	Q	P_{TC}	$|V_{TC}|$	$|Z_{34IN}|$	CF (dB)	f_r (GHz)
EXP	11.6616	0.0012	0.1596	1045.1	-30.5853	0.6764
HFSS (fitted)	12.2407	0.0015	0.1760	999.3692	-31.2705	0.6610
HFSS (unfitted)	51.23	0.0046	0.8431	7800.8	-32.96	0.6660

Chapter 8 Conclusion & Future Work

A study of the dependence on geometry of the electrical performance characteristics of an intra-coaxial transmission line coupler was performed. Four different geometric features of the TXC were varied in the study. These features are loop surface area, loop aspect ratio, trace thickness, and separation distance between the loop and the coax center conductor. This study involved designing and fabricating a series of experimental TXC test structures and mounting each test structure inside a customized DIN 7/16 inline adapter to form a TXC test fixture. The four port S-parameters of each test fixture were then measured using a vector network and simulated using a high frequency structure simulator (HFSS). Six electrical performance factors were computed from experimental data and from HFSS simulations. The performance factors are power transfer characteristic (P_{TC}), voltage transfer characteristic (V_{TC}), Q-Factor, resonant impedance at the TXC terminals ($|Z_{34IN}|$), resonant frequency (f_r), and Coupling Factor (CF).

Experimental results can be summarized as follows:

1) Larger TXC loop surface area corresponds to higher CF, lower f_r (assuming fixed tuning capacitor), higher Q-Factor, higher P_{TC}, higher $|V_{TC}|$, and lower $|Z_{34IN}|$.

2) Larger separation distance between the TXC loop and the coax center pin corresponds to higher CF, higher f_r, lower $|Z_{34IN}|$, lower Q Factor, lower $|V_{TC}|$, and lower P_{TC}.

3) Larger trace thickness corresponds to lower the Q-Factor, lower $|Z_{34IN}|$. The $|V_{TC}|$, P_{TC}, CF and f_r are relatively insensitive to trace thickness.

4) Q-Factor, P_{TC}, $|Z_{34IN}|$, $|V_{TC}|$, CF, and f_r are all relatively insensitive to the aspect ratio.

Of the six performance factors computed from the HFSS simulations, only f_r and CF seemed to agree roughly with results obtained from experimental data. Computation of Q-Factor, P_{TC}, $|Z_{34IN}|$ and $|V_{TC}|$ from HFSS simulations yielded significantly lower values than the values computed from

experimental data. It was hypothesized that this discrepancy was due to the use of standard copper as the TXC trace conductor in the HFSS simulations. Surface metallization in the experimental TXC structures was formed by the LDS process which presumably leads to traces with much lower conductivity than that of standard copper. HFSS simulations were repeated for one TXC test structure using more realistic trace conductivity. The agreement between performance factors computed from experimental data and from the "fitted" HFSS simulations was significantly improved.

Future Work:

The first improvement to be done would be to repeat the experiments with much higher resolution focused around the resonance. Presumably this would allow a more accurate calculation of all electrical performance parameters including the Q-factor. In addition, use of more realistic materials properties should lead to more accurate HFSS simulations.

The next improvement would be to carry out a more exhaustive study on the effects of geometry on electrical performance characteristics of the TXC. The variety of geometric features of TXC structures included in this study was admittedly limited. A wider range of structures would provide a more complete understanding of the relationship between TXC design and electrical performance.   Key design parameters that describe the RF behavior of the TXC structures are the P_{TC}, V_{TC}, Z_{34IN}, Q-Factor, Coupling Factor, and f_r. If a large enough number of structures were studied, it is possible that a nomograph, or lookup table, could be developed that would relate design parameters to RF performance. This would lead to the ability to design rapidly a large number of structures. Only a few RF measurements would then be required to confirm predicted viability of the structures.

These improvements in the understanding of the TXC should also assist in the development of the compact mathematical model described in [11]. This model treats the TXC as a simplified, highly idealized structure. It requires a number of parameters that must be obtained by fitting spectral S-parameter data generated by the model to data obtained from either experiment or HFSS simulations. More detailed knowledge of the effects of variation of parasitics, dielectric substrate, and geometry on the

electrical characteristics of the TXC structures should lead to improvements in the mathematical model. For example, the lookup table mentioned in the preceding paragraph could be used to establish a relationship between TXC design and model parameters. The resulting compact model could then be used to compute electrical performance factors directly from the TXC geometrical structure. This would represent a useful engineering model that could be used to design TXC devices.

Bibliography

1. Yen-Sheng Chen; Shih-Yuan Chen; Hsueh-Jyh Li; , "Analysis of Antenna Coupling in Near-Field Communication Systems," *Antennas and Propagation, IEEE Transactions on* , vol.58, no.10, pp.3327-3335, Oct. 2010

2. Langer, J.; Saminger, C.; Grunberger, S.; , "A comprehensive concept and system for measurement and testing Near Field Communication devices," *EUROCON 2009, EUROCON '09. IEEE* , vol., no., pp.2052-2057, 18-23 May 2009

3. Yaghjian, A.; , "Efficient computation of antenna coupling and fields within the near-field region," *Antennas and Propagation, IEEE Transactions on* , vol.30, no.1, pp. 113- 128, Jan 1982

4. Zargham, M.; Gulak, P. G.; , "Maximum Achievable Efficiency in Near-Field Coupled Power-Transfer Systems," *Biomedical Circuits and Systems, IEEE Transactions on* , vol.6, no.3, pp.228-245, June 2012

5. Aroor, S.R.; Deavours, D.D.; , "Evaluation of the State of Passive UHF RFID: An Experimental Approach," *Systems Journal, IEEE* , vol.1, no.2, pp.168-176, Dec. 2007

6. Moghe, R.; Yi Yang; Lambert, F.; Divan, D.; , "A scoping study of electric and magnetic field energy harvesting for wireless sensor networks in power system applications," Energy Conversion Congress and Exposition, 2009. ECCE 2009. IEEE , vol., no., pp.3550-3557, 20-24 Sept. 2009

7. Bouchouicha, D.; Latrach, M.; Dupont, F.; Ventura, L.; , "An experimental evaluation of surrounding RF energy harvesting devices," Microwave Conference (EuMC), 2010 European , vol., no., pp.1381-1384, 28-30 Sept. 2010

8. Rathi, D.; Singh, R.; Kulkarni, S.V.; , "Design, fabrication and testing of pressurized co-axial directional coupler for high RF power measurements for SST-1 ICRH system," *Recent Advances in Microwave Theory and Applications, 2008. MICROWAVE 2008. International Conference on* , vol., no., pp.590-592, 21-24 Nov. 2008

9. Wan-Kyu Kim; Moon-Que Lee; Jin-Hyun Kim; Hyung-sun Lim; Jong-Won Yu; Byung-Jun Jang; Jim-Seok Park; , "A Passive Circulator with High Isolation using a Directional Coupler for RFID," *Microwave Symposium Digest, 2006. IEEE MTT-S International* , vol., no., pp.1177-1180, 11-16 June 2006

10. Sophocles J. Orfanidis, "Electromagnetic Waves and Antenna," ECE Department Rutgers University, 1996.

11. Revelli, Joseph; Bowman, Robert; ,"Transmission Line Model for an Intra-Coaxial Transmission Line Coupler." ADIML Internal Document.

12. Rosa, E.B. (1908). "The Self and Mutual Inductances of Linear Conductors". *Bulletin of the Bureau of Standards* **4** (2): 301–344.

13. Marrocco, G.; , "The art of UHF RFID antenna design: impedance-matching and size-reduction techniques," *Antennas and Propagation Magazine, IEEE* , vol.50, no.1, pp.66-79, Feb. 2008 doi: 10.1109/MAP.2008.4494504

14. N. Heininger, J. Wolfgang, J. BoBler, "Manufacturing of Molded Interconnect Devices from Prototyping to Mass Production with LASER Direct Structuring" http://www.lpkf.com/_mediafiles/1277-mechatronic-component-for-automatic-steering-wheel.pdf